Mon. Not. R. Astron. Soc. **000**, 000–000 (2016) Printed 17 November 2016 (MN LATEX style file v2.2)

Emission-line stars in M31 from the SPLASH and PHAT surveys

Laura J. Prichard[1⋆], Puragra Guhathakurta[2], Katherine M. Hamren[2], Julianne J. Dalcanton[3], Claire E. Dorman[2], Anil C. Seth[4], Benjamin F. Williams[3], Gabriel A. Damon[5], Anita Ilango[6], Megha Ilango[6]

[1]*Sub-department of Astrophysics, Department of Physics, University of Oxford, Denys Wilkinson Building, Keble Road, Oxford OX1 3RH, UK*
[2]*UCO/Lick Observatory, University of California Santa Cruz, 1156 High Street, Santa Cruz, CA 95064, USA*
[3]*Department of Astronomy, Box 351580, University of Washington, Seattle, WA 98195, USA*
[4]*Department of Physics & Astronomy, University of Utah, Salt Lake City, UT 84112, USA*
[5]*Santa Cruz High School, 415 Walnut Avenue, Santa Cruz, CA 95060, USA*
[6]*Cupertino High School, 10100 Finch Avenue, Cupertino, CA 95014, USA*

arXiv:1611.05043v1 [astro-ph.SR] 15 Nov 2016

Accepted 2016 November 15. Received 2016 November 11; in original form 2016 September 8

ABSTRACT

We present a sample of 224 stars that emit Hα (Hα stars) in the Andromeda galaxy (M31). The stars were selected from $\sim$ 5000 spectra, collected as part of the Spectroscopic and Photometric Landscape of Andromeda's Stellar Halo survey using Keck II/DEIMOS. We used six-filter *Hubble Space Telescope* photometry from the Panchromatic Hubble Andromeda Treasury survey to classify and investigate the properties of the Hα stars. We identified five distinct categories of Hα star: B-type main sequence (MS) stars, 'transitioning'-MS (T-MS) stars, red core He burning (RHeB) stars, non-C-rich asymptotic giant branch (AGB) stars, and C-rich AGB stars. We found $\sim$ 12 per cent of B-type stars exhibit Hα emission (Be stars). The frequency of Be to all B stars is known to vary with the metallicity of their environment. Comparing this proportion of Be stars with other environments around the Local Group, the result could indicate that M31 is more metal rich than the Milky Way. We predict that the 17 T-MS Hα stars are Be stars evolving off the MS with fading Hα emission. We separated RHeB from AGB Hα stars. We conclude that the 61 RHeB and AGB stars are likely to be Long Period Variables. We found that $\sim$ 14 per cent of C-rich AGB stars (C stars) emit Hα, which is an upper limit for the ratio of C-rich Miras to C stars. This catalogue of Hα stars will be useful to constrain stellar evolutionary models, calibrate distance indicators for intermediate age populations, and investigate the properties of M31.

Key words: *(galaxies:)* Local Group – galaxies: stellar content – stars: emission-line, Be – stars: AGB and post-AGB –stars: variables: general – surveys.

1 INTRODUCTION

Studying stellar populations in different environments in the Local Group (LG) is essential for advancing our knowledge of stellar evolution. Understanding the different stages of evolution for massive and intermediate mass stars under a variety of initial and environmental conditions is crucial for constraining stellar evolutionary models. Emission lines arising from different types of stars are powerful diagnostic tools for determining their physical conditions. The Hα line, an emission line in the Balmer series of hydrogen at 6563 Å, is among the most useful due to the abundance of hydrogen in the universe. This emission line can arise from multiple processes and in many types of stars. Conducting a survey of stars that exhibit Hα emission (Hα stars) can give us insights in to some of these lesser-known stages of stellar evolution. The analysis of Hα stars can also tell us about the properties of their environment, galaxy evolution, and even be used as distance indicators.

Hα emission is typically associated with the brightest stars such as B-type main sequence (MS) stars. B stars have the maximum rotational velocity compared to other stellar classes, with typical values of $\sim$ 200 km s^{-1} (McNally

⋆Email: Laura.Prichard@physics.ox.ac.uk

© 2016 RAS

1965). They have temperatures of 10,000–30,000 K and a mass range of 3 $M_\odot$ < M < 20 $M_\odot$. They are short lived and because of this, they are often associated with a parent cloud or nebulous regions of the interstellar medium (ISM), so-called HII regions. Beyond temperatures of around 10,000 K, hydrogen is ionized so Hα absorption and emission should not be seen. However, studies show that for rapidly rotating massive stars, Hα emission arises from material in a rotationally flattened envelope that creates a circumstellar disc (e.g. Struve 1931; Dougherty & Taylor 1992) or accreted material that forms a disc. B-type stars that have exhibited Hα emission at least once are classified as Be stars (Jaschek et al. 1980). As discussed in the review by Porter & Rivinius (2003), whether the Be phase is an evolutionary stage of all B-type stars is still contested.

Surveys of Be stars have shown that their environment can affect their frequency; lower metallicity environments have a higher proportion of Be stars (e.g. Maeder, Grebel & Mermilliod 1999; Martayan et al. 2007). It is thought that stars rotate faster in lower metallicity environments, perhaps due to weaker magnetic coupling of the star with its surroundings from formation, causing more of them to exhibit emission lines originating from their rotationally flattened envelope (Maeder, Grebel & Mermilliod 1999; Wisniewski & Bjorkman 2006; Martayan et al. 2007). As well as the metallicity dependence on the proportion of Be stars, it was also suggested that there could be some evolutionary dependence on their frequency (e.g. Schild & Romanishin 1976; Tarasov & Malchenko 2012). The age of star clusters was found to affect the frequency of Be stars, and it was concluded that the Be phase was an evolutionary stage of all B stars that occurs at $\sim$ 10 Myr (Fabregat & Torrejón 2000). This discovery could mean that there is an age-metallicity degeneracy for the environments of Be stars. More studies of the properties of Be stars and their environments are needed to better understand the evolution of massive MS stars and put constraints on the processes that occur within them.

The evolutionary path a star takes off the MS is dependent on its mass (e.g. Hayashi, Nishida & Sugimoto 1962, and references therein). For intermediate- to high-mass stars ($\sim$ 3.5–15 $M_\odot$), He burning (HeB) begins in a non-degenerate core (e.g. Gallart, Zoccali & Aparicio 2005, and references therein). The star becomes more luminous and red, and populates the red core HeB (RHeB) branch in colour-magnitude space (e.g. Dohm-Palmer & Skillman 2002; McQuinn et al. 2011). Stars traverse the colour-magnitude diagram (CMD) blue-ward during their HeB lifetime, completing a 'blue loop' before moving red-ward again towards the RHeB sequence (e.g. Stothers & Chin 1968). The bluest point in a star's 'blue loop' phase defines the blue core HeB (BHeB) branch on a CMD (e.g. Bertelli et al. 1994). Low- to intermediate-mass stars ($\sim$ 0.8 to $\lesssim$ 3.5 $M_\odot$) at the end of their red giant branch (RGB) phase, ignite He in their degenerate core in a He flash, moving on to the horizontal branch on a CMD. Once core He is depleted, both low- and high-mass stars (up to $\sim$ 8 $M_\odot$), move up their Hayashi line with increasingly convective envelopes (Hayashi & Hoshi 1961), and a star is then in the asymptotic giant branch (AGB) phase of evolution.

Some AGB stars can exhibit Hα emission. AGB stars have masses 0.8 $M_\odot$ < M < 8 $M_\odot$, they have C-O cores and are burning H/He in their shells. Despite the different evolutionary tracks taken by stars of different masses, both low- to high-mass MS stars evolve on to the AGB. It is during the AGB phase that a star loses most of its mass, transforming in to a planetary nebula (e.g. Iben 1974; Iben & Renzini 1983). Towards the end of the AGB phase, a star will experience a series of thermal pulses (TP-AGB phase) that arise from instabilities in the H/He burning shells (Schwarzschild & Härm 1965). These stars have convective envelopes and atmospheres of atomic and molecular gas, and dust (e.g. Schwarzschild & Härm 1967; Iben 1974). Studying the mass loss in these stars helps us to understand the metal enrichment of the ISM (e.g. Gehrz 1989; Blum et al. 2006).

In general, AGB stars are categorised as being oxygen rich (C/O < 1), M-type stars (M stars), or carbon rich (C/O > 1), C-type stars (C stars). This carbon excess is caused by the 'third dredge-up' that occurs during the TP-AGB phase, bringing carbon to the surface (see Iben & Renzini 1983, and references therein). The transition from oxygen to carbon rich is known to depend on the metallicity of the environment and stellar mass (e.g. Iben 1974; Karakas, Lattanzio & Pols 2002; Battinelli & Demers 2005). C stars have increased opacity due to the presence of CN in their atmospheres, this leads to a substantial increase in their mass loss (e.g. Marigo 2002; Mattsson, Wahlin & Höfner 2010; Sandin, Roth & Schönberner 2010). C-rich stars also tend to be more luminous at redder wavelengths than their non-C-rich counterparts (e.g. Frogel, Persson & Cohen 1980; Frogel, Mould & Blanco 1990). Studying populations of C stars is useful to constrain models of AGB stars (Karakas 2014), understand their role in the enrichment of the ISM (e.g. Boyer et al. 2011), and study the metallicity gradients of their environments (e.g. Cioni et al. 2008; Feast, Abedigamba & Whitelock 2010).

Long Period Variables (LPVs) are AGB stars that undergo long-period pulsations and exhibit Hα emission (e.g. Merrill 1921, 1952). LPVs typically exhibit strong Balmer emission for around 90 per cent of their cycle, however these line strengths can vary between cycles (e.g. Joy 1954). The pulsations in LPVs arise from shock waves in the lower photosphere of the star and result in shock-excited Hα emission (e.g. Bowen 1988). LPVs can be split in to two main categories, semiregular variables (SRs) and Mira variables (Miras)[1]. These stars have pulsation periods of $\sim$ 100–1000s of days, with the average period of Miras being longer than SRs by a factor of two, although there is significant overlap (e.g. Wood & Cahn 1977; Hughes & Wood 1990).

SRs and Miras share many common characteristics and it is now accepted that SRs are the progenitors of Miras (e.g. Lloyd Evans & Menzies 1973; Whitelock 1986). In many cases the SR and Mira classifications overlap and they are often misidentified due to their restrictive classical definition (e.g. Kerschbaum & Hron 1992). Studies of Miras and SRs usually involve multi-epoch observations of their photometric properties to distinguish between the two types. Miras tend to have larger amplitude magnitude fluctuations (ΔI $\sim$ 2.5) compared to SRs (ΔI $\sim$ 0.5; e.g. Hughes 1989; Wood & Sebo 1996). Miras typically have a regular pulsa-

[1] We use the term Mira variables to mean AGB stars with long-period, large-amplitude pulsations (see Whitelock, Feast & Catchpole 1991).

tion period, while SRs have intermittent regularity as their name implies (e.g. Feast 1996; Wood 2000). The two types of LPV also occupy distinct regions of K-band and period (logP) space (e.g. Feast et al. 1989; Hughes & Wood 1990). To correctly classify Miras from other LPVs, K magnitude light curves are essential (e.g. Battinelli & Demers 2014).

Miras have a period-luminosity relation that makes them ideal distance indicators (e.g. Glass & Evans 1981; Glass & Feast 1982), particularly when observed in the infrared (Whitelock 2013). These older stars are in the haloes of galaxies and can be more easily resolved than those in the discs of spirals. Observing them in the infrared avoids contamination from ISM extinction. Miras are the ideal candidates for distance measurements, but so far, large spectroscopically confirmed samples of Mira variables have been difficult to obtain in external galaxies due to instrument limitations. Identifying large samples of Miras spectroscopically will help us to calibrate them for use as standard candles of intermediate-age stars. As Miras are AGB stars, they too can be defined as either C or O rich. Models of C-rich Mira variables (C-Miras) are well constrained (Arndt, Fleischer & Sedlmayr 1997; Wachter et al. 2002; Sandin, Roth & Schönberner 2010). In addition to having well developed models, this population of stars possesses both the environmental dependence of C stars (e.g. Karakas, Lattanzio & Pols 2002) with the standard candle benefits of Mira variables (Glass & Evans 1981), making them valuable probes of galactic environments.

Investigating populations of C-Miras in different environments has been the focus of a recent study (see Battinelli & Demers 2014, and references therein). C-Miras presented in the study were identified by photometrically monitoring variations in spectroscopically confirmed C stars. To identify C-Miras in previous studies, C star catalogues were cross-matched with variable star surveys. Compiling data from the literature, it was shown that the proportion of C-Miras to all C stars (C-Mira/C star) was around 12 per cent in many extra-galactic systems (NGC 6822, NGC 147, NGC 185, Fornax dwarf galaxy, and Leo 1). Looking at data for the Large Magellanic Cloud (LMC; Cioni et al. 2001; Cioni & Habing 2003), a C-Mira/C star value of < 22 per cent was found (Battinelli & Demers 2014). This upper limit for the LMC arose due to limitations of the sample and the value could be down to 12 per cent as seen in other systems. However, the Milky Way (MW) halo has a significantly larger C-Mira/C star fraction of 40 per cent (Mauron et al. 2014), and this value was recalibrated and expected to be up to 50 per cent (Battinelli & Demers 2014). When comparing this C-Mira/C star proportion with the Sagittarius dwarf spheroidal galaxy (Sgr dSph), a tidally disrupted galaxy in the MW halo (Ibata, Gilmore & Irwin 1994), a similar proportion of 48 per cent was found (Battinelli & Demers 2013). Why the C-Mira/C star proportion in the halo of our galaxy and Sgr dSph differs appreciably from the 12 per cent found in other galaxies is not clear. Currently there is no comparative C-Mira/C star value for the Andromeda galaxy (M31), which is similar to the MW in morphology and mass, to investigate this difference further.

Given its relative proximity, around 785 ± 25 kpc (McConnachie et al. 2005), M31 provides an ideal test bed for investigating the properties of stars with Hα emission. With the advantage of an external view of a spiral galaxy with a vast range of environments and stellar types to survey, a range of astrophysical research is possible. Many large surveys of Hα stars have been performed throughout the LG. These surveys included regions of the Small Magellanic Cloud (SMC) and LMC (e.g. Henize 1956; Bohannan & Epps 1974; Azzopardi & Meyssonnier 1986; Pereira et al. 2001; Martayan et al. 2011; Reid & Parker 2012), Galactic environments (e.g. Downes & Keyes 1988; Kun 1992; Miszalski, Mikołajewska & Udalski 2013) and some larger extragalactic systems such as M33 (e.g. Sholukhova, Fabrika & Vlasyuk 1999). Extensive narrowband photometric coverage of M31 and M33 detected only the most massive Hα stars (Massey et al. 2006). Thus, there remains a distinct lack of data and comparative statistics of the full Hα star population of M31.

With spectra from the Keck II telescope collected as part of the Spectroscopic and Photometric Landscape of Andromeda's Stellar Halo (SPLASH) project (Dorman et al. 2012), we have been able to spectroscopically identify individual Hα stars in M31. Using supporting six-filter *Hubble Space Telescope* (HST) photometry from the Panchromatic Hubble Andromeda Treasury (PHAT) survey (Dalcanton et al. 2012), we have analysed and classified Hα stars in M31. Details of the two data sets used in this paper are given in §2. The algorithm and selection conditions to obtain our sample of Hα stars is outlined in §3. The classification and analysis of the Hα star sample using photometry, emission-line properties, and distribution is described in §4. A discussion of the scientific results and their significance is covered in §5. We present a summary of our findings in §6.

2 DATA

To investigate emission-line stars in M31, we used two complementary data sets. To classify and analyse our selected Hα stars we used photometric data from the PHAT survey, detailed in §2.1. To select the emission-line stars and determine their properties, we analysed a spectroscopic sample from the SPLASH survey, described in §2.2.

2.1 Photometric data

The PHAT survey is a multi-cycle HST program. The survey covers around a third of M31's disc in six filters that span from ultraviolet (UV) to near-infrared (NIR). With HST's observing capabilities, the disc of M31, out to 20 kpc, is resolved in to more than 100 million stars. Dalcanton et al. (2012) chose to observe the northeast quadrant of M31 as it has the least obscured active star forming regions and least extinction. The spatial coverage selected by the PHAT team also maximised the range of environments and thus stellar evolutionary stages observed. They used two UV filters (F275W and F336W), one optical filter (F475W), one far-red filter (F814W), and two NIR filters (F110W and F160W). The filters were chosen to constrain extinction and effective temperature of a range of stellar populations. Different age stellar populations were identified by comparison with artificial CMDs generated using the six filters. Details of the observations, data reduction, and production of six-filter photometric catalogues of stars with accurate astrometry are given in Dalcanton et al. (2012), and Williams et al. (2014). The PHAT survey provides a large and multidimensional

catalogue of data that enables the classification of objects based on colour.

2.2 Spectroscopic data

To select Hα stars, we used a spectroscopic sample that was collected as part of the SPLASH survey. Although the initial aim of the SPLASH project was to characterise the halo of M31, in recent years it has focussed on the disc and inner regions. In this latest phase of the survey, the crowded disc-dominated region of M31 observed by the SPLASH team was chosen to overlap with the PHAT survey coverage. The data analysed in this paper comes from this crowded, northeast quadrant of M31 where the two surveys overlap. The spectroscopic targets were selected from the PHAT catalogue to span a range of stellar ages including MS, AGB, and RGB stars (Dorman et al. 2015). All stars had apparent magnitudes greater than F814W = 22 or F475W = 24 to ensure good quality spectra could be obtained of the fainter targets. The isolation of each star was taken into account in order to reduce possible contamination from neighbouring stars (see Dorman et al. 2012).

The spectra were reduced using the SPEC2D and SPEC1D software (Cooper et al. 2012; Newman et al. 2013) that were modified for the SPLASH survey. SPEC2D extracted a one-dimensional spectrum from the two-dimensional data, SPEC1D then calculated redshifts for each spectrum by comparing it to spectral templates. Dorman et al. (2012) describe the full data reduction of the spectroscopic sample.

Hamren et al. (2015) used this spectroscopic sample to identify C stars in order to investigate the C-star to M-star ratio in M31. To identify AGB C stars, they used a χ^2 comparison, position in CN − TiO, and F475W − F814W colour-colour space. Within the 5295, 600 line mm^{-1} SPLASH spectra, they identified 83 C stars. We later use this sample to identify any C stars among our sample of Hα stars and for comparison to other studies in the discussion of AGB Hα stars in §5.4.

3 SAMPLE SELECTION

To select a sample of Hα stars, we used the 1D SPLASH spectra described in §2.2. The 2D spectra from the SPLASH survey were used in this study only to verify the result of our detection algorithm performed on the 1D spectra. The list of emission-line sources that we used to check the efficiency of the algorithm used to find Hα stars, was determined from visual inspection of $\sim$ 1/3 of the total 5295, 600 line mm^{-1} 2D spectra. The 2D spectra can be useful for determining the nature of the emission, i.e. if from the star or a nebulous region of ionised gas. An automated detection algorithm for the 2D spectra will therefore be the focus of future work using the SPLASH sample but beyond the scope of this paper. For an example of 2D SPLASH spectra of four stars, two classified as Hα stars and two with nebulous Hα emission, see Appendix B.

3.1 Selecting the data subset

From the sample of 5295 SPLASH spectra, we wanted to ensure that each Hα star was selected in the same way in order to produce a uniform sample. To do this we used a subset of data from which to select our sample. We ensured each spectrum in the subset was a stellar object, based on a previous classification, and had data in all of the sections that the selection algorithm used to identify Hα stars.

Some of the spectra in the sample were previously identified as X-ray sources. Some LPVs can be 'symbiotic stars', evolved giants that are accreting on to a compact companion, typically a white dwarf (e.g. Warner 1972; Allen 1984). Symbiotic stars cannot be compared easily alongside isolated LPVs due to their interaction, as emission may arise from both the LPV and compact companion. As white dwarfs are UV bright and often emit in the X-ray, we decided that where possible we would try to avoid symbiotic stars by not including these X-ray sources. Finally, some objects were previously identified by PHAT as star clusters, and we were only interested in individual stars. For consistency in the data subset, we removed the previously identified X-ray sources and PHAT star clusters, leaving 5121 stellar spectra.

As well as the Hα line, some of the spectra also exhibited other emission lines including some forbidden lines of nitrogen and sulphur: [NII]a,b λ6548,6583 and [SII]a,b λ6716,6731. These lines are typically associated with diffuse HII regions that are markers for massive star formation. They are also found in planetary nebulae (PNe), and much less frequently in some hot MS stars that experience strong stellar winds. B-type stars with forbidden emission lines are called B[e] stars. Although B[e] stars can exhibit these lines, they are hard to distinguish from hot stars surrounded by ionised ISM. To minimise the chance of selecting a star in an HII region, rather than an Hα star, or an object that emits [NII] and [SII] lines such as a PNe, these lines were tested for. To calculate root-mean-squared (RMS) noise values of the spectra, we used a region of continuum red-ward of the Hα line between 6600 and 6640 Å. Fitting a straight line and taking the standard deviation (STDEV) of the data to the line gave the RMS value, and thus a measurement of the noise for each spectrum. To ensure that every spectrum in our sample had undergone a similar selection process, we removed spectra that had data missing in any of the key areas we analysed. If any spectrum did not have data in the Hα/[NII] region, the [SII] region, or the region to measure continuum, these spectra were omitted. This left a subset of 4686 spectra from which we selected our Hα star sample.

3.2 Selection algorithm

We developed a selection algorithm for finding emission-line stars from the 1D spectroscopic SPLASH data. The spectra had been shifted to the rest frame and their respective velocities were given by SPEC1D. To begin our analysis of each spectrum, we normalised each of the 4686 subset of spectra by dividing by the continuum level local to the Hα line. To guide the selection process and to verify the efficiency of the selection algorithm, we used the list of emission-line sources visually identified from a subsample of the 5295 2D SPLASH spectra.

To measure the properties of spectral features, we fitted Gaussian curves to each 1D spectrum of the 4686 spectra in the data subset. A double Gaussian curve was used to fit the Hα λ6563 and [NII]b λ6583 lines. In the narrow region of the spectrum between $\sim$ 6540–6590 Å, there are three emission

lines, Hα and the two [NII] lines. We adopted the fixed ratio of [NII]a,b lines as 1:3 (Osterbrock 1989). As the [NII]b line is stronger, we opted to fit only that and the Hα using a double Gaussian to reduce the number of model parameters the program was trying to optimise. We fitted for both the Hα and [NII]b lines, and the slope of the local continuum simultaneously using Eq. 1. We also used this method for fitting the [SII]a,b lines.

$$f_{dG}(x) = \frac{A_1}{\sigma_1\sqrt{2\pi}} \exp\left(-\frac{(x-\lambda_1)^2}{2{\sigma_1}^2}\right) + \frac{A_2}{\sigma_2\sqrt{2\pi}} \exp\left(-\frac{(x-(\lambda_1+\delta\lambda))^2}{2{\sigma_2}^2}\right) + (mx+c)\,. \quad (1)$$

Here A_1 and A_2 are the peak amplitudes, and σ_1 and σ_2 are the line widths for the two peaks, either Hα and [NII]b or [SII]a,b. λ_1 is the central wavelength of the first line which was not fixed, but we used a constant wavelength separation ($\delta\lambda$) between the two lines being measured, this allowed for small shifts in velocity. The slope of the continuum was given by the gradient (m), and y-intercept (c). We found a double Gaussian was more reliable at fitting the data as it had less independent parameters than fitting individual Gaussians to each emission line. To account for lines of different widths, the ranges of the fits were chosen to cover wavelengths of 6553 - 6593 Å for the Hα and [NII]b lines, and 6706 - 6741 Å for the [SII]a,b lines.

To find the best-fitting curve, the MPFITFUN routine[2], which utilises the Levenberg–Marquardt method was used. By visually inspecting the fits of many spectra, a set of initial parameters was given to MPFITFUN to ensure the best-fitting curve of this region. We did not fix any of the input values in Eq. 1 but we did find that the program was sensitive to initial values for each of the seven input model parameters. Specifically, we set a positive peak height and line width to encourage the program to find a line, we found the program could more easily recover emission this way if it was present.

To calculate emission-line strengths, we used equivalent widths (EWs); the strength of the line relative to the continuum. We summed over each of the emission lines separately. Using Eq. 2, an emission line has a negative EW value:

$$EW \approx \sum_{i=1}^{N} \left(1 - \frac{f_{dG}(x_i)}{F_0}\right) \cdot \Delta\lambda. \quad (2)$$

Here, N is the number of wavelength intervals, $f_{dG}(x_i)$ is the value of the double Gaussian fit for each wavelength channel, and $\Delta\lambda$ is the resolution of each wavelength channel in Angstroms. The constant continuum level F_0 was obtained from the average continuum level over the wavelength range of the fit. To quantify the goodness of the fit for each channel, the reduced χ^2 was calculated as follows:

$$\frac{\chi^2}{N} = \frac{1}{N}\sum_{i=1}^{N} \frac{(F_i - f_{dG}(x_i))^2}{\sigma^2}. \quad (3)$$

Here, F_i is the flux in each wavelength channel and σ^2 is the variance of the data. We found this a useful test of how well the model fit the data and thus the reliability of the measured parameters.

[2] Developed by C. Markwardt for Interactive Data Language (IDL).

3.3 Selection criteria

Using the set of parameters determined in §3.2, we wanted to identify stars with significant Hα detection. To ensure we selected a clean Hα star sample, we also wanted to omit objects with significant [NII]b or [SII]a,b emission. To identify Hα stars reliably and automatically from the data subset, we chose selection criteria. To find the optimum set of criteria, the objects selected by the algorithm were compared to the visually selected subsample of Hα stars, as determined from the 2D spectra, to determine its ability to find Hα stars from the 1D spectra. We chose the following set of criteria (numbers 1–5) to be lenient (around 2.5σ accuracy). This combination of constraints produced a list of Hα stars with $\sim$ 5 per cent contamination. The final criterion was a visual inspection, if the algorithm had falsely identified Hα or had failed to detect [NII] or [SII] emission, we removed the star from our final sample. The criteria used, their order, and their efficiency of removing non-Hα stars is detailed below.

1. Hα EW value $< -2.5 \times \Delta$EW $\longrightarrow$ removed 2816 stars
2. Hα peak height $> 2.5 \times$ RMS $\longrightarrow$ removed 357 stars
3. [NII]b peak height $< 2.5 \times$ RMS $\longrightarrow$ removed 84 stars
4. Hα & [NII]b Gaussian $\frac{\chi^2}{N} < 0.62 \longrightarrow$ removed 38 stars
5. [SII]b peak height $< 2.5 \times$ RMS, for [SII]a,b Gaussian $\frac{\chi^2}{N} < 0.62$ OR [SII]b peak height $< 4 \times$ RMS, for [SII]a,b Gaussian $\frac{\chi^2}{N} > 0.62 \longrightarrow$ removed 15 stars
6. Visual inspection $\longrightarrow$ removed 12 stars

This set of criteria produced a sample of 229 Hα stars, $\sim$ 5.5 per cent of the total sample. By comparing our selected sample with the visually selected list we were able to verify the algorithm's efficiency of selecting Hα stars. For a full list of selected Hα stars, their coordinates, and determined properties, see the catalogue in Appendix A.

4 DATA ANALYSIS

With a sample of 229 Hα stars selected, we used the six-filter HST photometry and their measured parameters from the selection algorithm to classify them and investigate their properties.

4.1 Hα star photometry

CMDs of the PHAT photometry are shown in Fig. 1. The small points are of the objects in the sample of 5295 SPLASH spectra that have data in the relevant HST filters. We have separated them in to four categories. The small crosses are serendipitously observed sources ('serendips'), the grey points are all sources with poor spectral quality

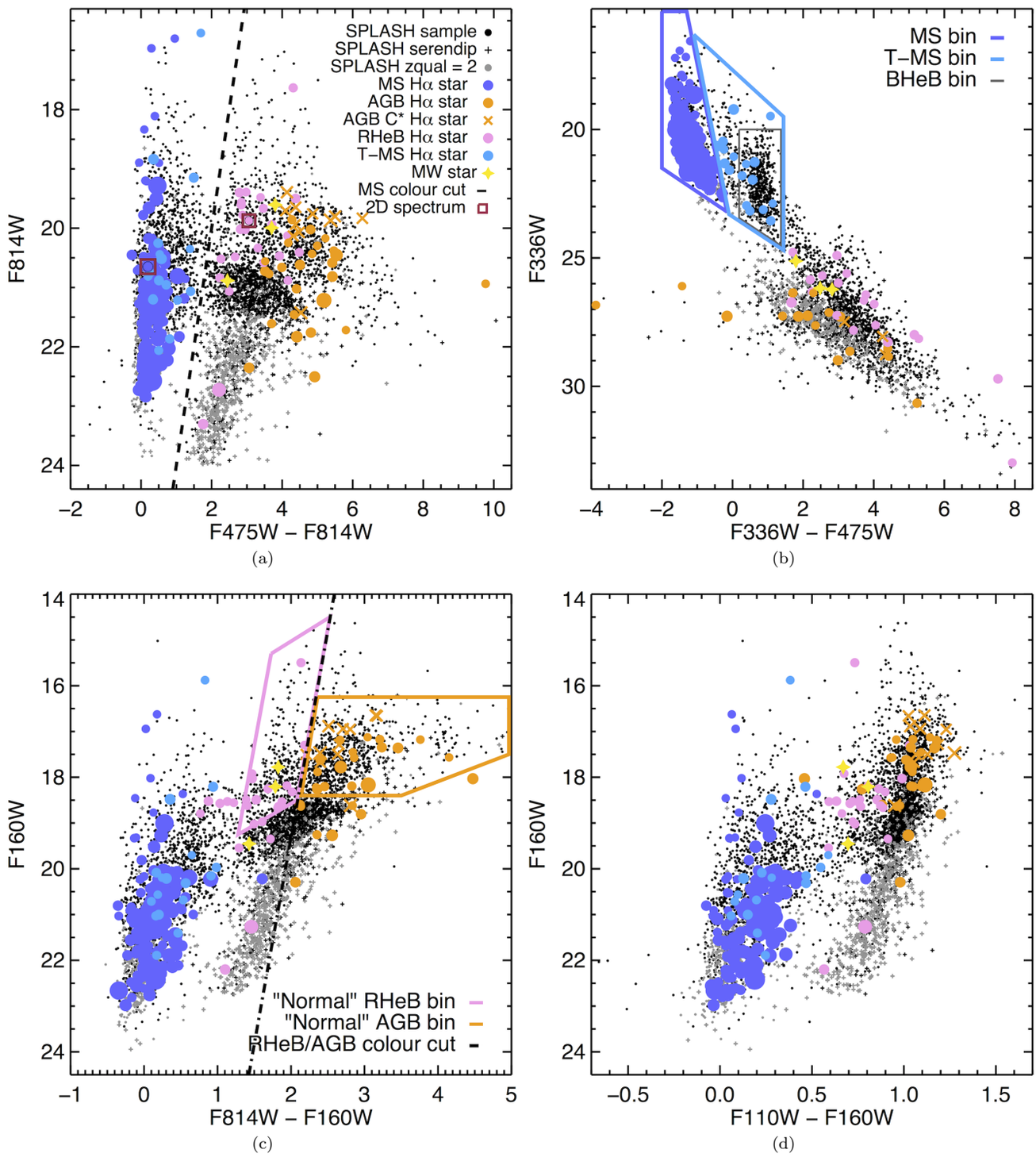

Figure 1. CMDs of PHAT photometry. Small points are the 5295 SPLASH objects, including serendipitously observed sources 'serendips' (small crosses), and sources with poor spectral quality (zqual = 2; grey points). Larger points are Hα stars; their size indicates Hα emission-line strength (|EW|), their 'normal' population is defined by their respective polygons. Yellow points, not scaled to line strength, are foreground MW Hα stars. (a) The optical colour cut (black dashed line) separates the blue and red Hα stars. Examples of the 2D SPLASH spectra of Hα stars in red boxes are shown in Appendix B. (b) We distinguish regular MS stars (dark blue polygon), from the BHeB stars (thin grey polygon), and define T-MS Hα stars (pale blue polygon). (c) Redder Hα stars are separated in to RHeB and AGBs using a colour cut (Rosenfield et al. 2016; dot-dash line).

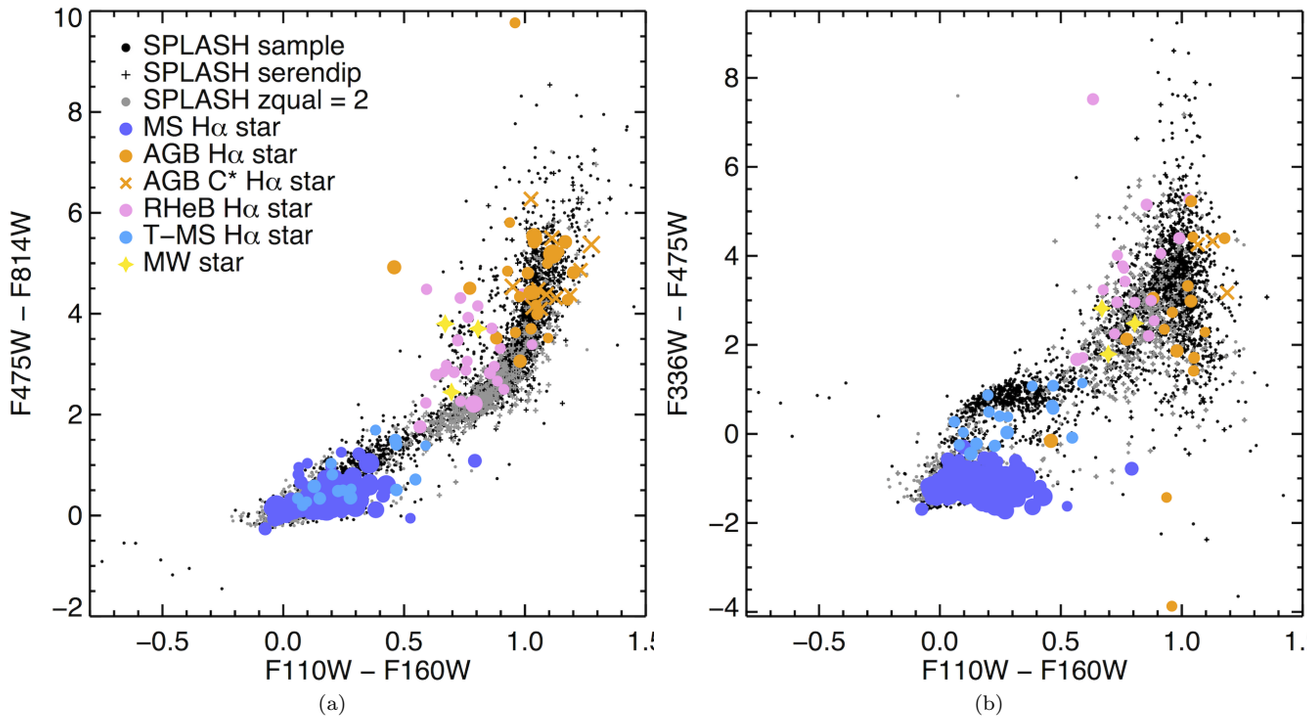

(a) (b)

Figure 2. 2CDs of the PHAT photometry follow the same labelling as Fig. 1. (a) 2CD of optical − far-red vs. NIR colours. (b) 2CD of UV − optical vs. NIR colours. Fewer redder stars appear as only ∼ 89 per cent of the Hα stars have F336W data. See §4.1.

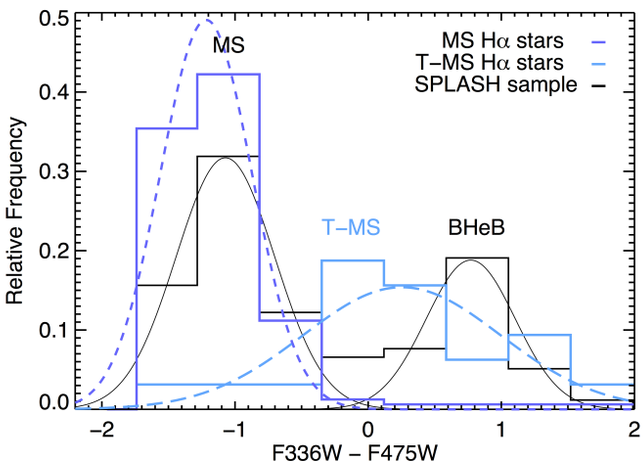

Figure 3. Histogram of relative frequencies of stars blue-ward of the optical colour cut in Fig. 1(a) vs. the UV − optical colour. Hα T-MS stars (light blue long-dashed Gaussian) are not associated with the MS or BHeB sequence. See §4.1.3.

(i.e. zqual = 2) and thus unreliable velocity measurements, the small grey crosses are both poor quality and serendips. The black points are the remaining objects in the SPLASH sample. The larger points represent the Hα stars that we selected, their symbol size is a measure of their Hα line-strengths (|EW|). In Fig. 1(a) are two Hα stars in red boxes. These stars correspond to the two Hα stars for which we present their 2D SPLASH spectra in Appendix B.

We take advantage of the HST photometry by plotting a range of CMDs that allow us to differentiate different stellar populations. Fig. 1(a) is an optical/far-red CMD of the F475W and F814W filters that does a good job of separating the blue and red stars in the SPLASH sample. We use an optical colour cut to define this separation, indicated by the dashed line. The RGB stars form a dense clump of black points between F475W − F814W ∼ 2–4 mag and centred on F814W ∼ 21 mag. The points below the RGB stars, mostly poor spectral quality grey points due to their faint magnitudes, are likely to be both RGB stars, and variable AGB or RHeB stars that are near minima in their cycles. Note that RGB stars do not exhibit Hα emission, so any Hα stars below the magnitude of the tip of the RGB (TRGB) are either variable AGB or RHeB Hα stars or some contamination from symbiotic stars. The UV/optical CMD (Fig. 1(b)) of the F336W and F475W filters separates the different varieties of bluer stars, while the far-red/NIR CMD Fig. 1(c) of the F814W and F160W filter is used to separate the redder stars. We show the NIR CMD of the F110W and F160W filters (Fig. 1(d)) and the colour-colour diagrams (2CDs) in Fig. 2 to show the distributions of the SPLASH sample and Hα stars in different CMD and 2CD spaces.

The Hα star photometry is included in the catalogue in Appendix A. Two of our selected Hα stars do not have PHAT photometry as these were serendips that were not in the PHAT catalogue. This left 227 Hα stars we were able to classify. Some of our selected Hα stars did not have data in all six filters. Many stars, mostly the redder RHeB and all AGB stars do not have data in the UV filter F275W. For some sources that were faint in F275W, the detection would have been noise, and so were deemed unreliable. We therefore chose a magnitude cut of F275W < 24.5 mag, leaving only 157 of 227 (∼ 69 per cent) Hα stars with reliable F275W

detections. Due to this large proportion, we decided not to include the F275W filter in our analysis for consistency. For the remaining five filters, the F336W filter has detections for 157 ($\sim$ 89 per cent), F475W and F814W have data for all, F110W has data for all but one, and F160W has data for all but two of the 227 Hα stars with PHAT photometry.

In the following section we describe the method for identifying MW Hα stars. The parameters for identifying the five classifications of Hα stars are described in the subsequent sections. A summary of values determined in these sections and additional average properties for each class are given in Table 1.

4.1.1 Removing foreground MW Hα stars

Identifying foreground MW stars required multiple diagnostics in order to separate them from the stars in M31. Low-mass old halo stars are most commonly confused with red massive stars at the distance of M31, such as the RHeB and AGB stars. In order to identify which Hα stars in our sample were foreground MW stars we used a combination of CMD space and spectral-line strengths. Using a set of visibly identified MW stars as a training sample, we plotted the SPLASH sample and the MW stars on two 2CDs; F336W $-$ F475W vs. F475W $-$ F814, and F814W $-$ F160W vs. F475W $-$ F814W. A third plot of the line strength (|EW|) of the surface gravity sensitive feature Na I λ8190–8900, used to distinguish low and high mass stars (Faber & French 1980), against the F475W $-$ F814W colour was also used. Using the known MW stars as a training set, polygons enclosing potential foreground contamination stars were drawn on the three separate plots. Stars that fell in all three of these polygons were classified as definite foreground MW stars. Of our Hα star sample, we identified three MW Hα stars, likely to be M-dwarf stars. We have marked these on the CMDs and 2CDs in Figs. 1 and 2 respectively (yellow stars). We remove these stars from our sample of Hα stars, leaving 224 in total, and do not include them in the analysis.

4.1.2 Classifying MS Hα stars

To identify the MS Hα stars we used the UV/optical (F336W and F475W) CMD in Fig. 1(b). Using this CMD, we were able to distinguish the MS stars from the BHeB stars in our sample (Dohm-Palmer et al. 1997). We used PAdova and TRieste Stellar Evolution Code (PARSEC) stellar evolutionary tracks (Bressan et al. 2012) to confirm the location of the MS stars in this CMD. The stars we identified as MS stars are enclosed in the dark blue polygon, drawn by eye and centred at F336W $-$ F475W ~ -1 mag. We therefore classify MS Hα stars as any Hα star within this MS bin, and the 'normal' MS population against which to compare the MS Hα stars, as any other SPLASH object within this bin. We found 146 MS Hα stars, $\sim$ 12 per cent of the MS population.

4.1.3 Classifying T-MS Hα stars

The bluer stars in the SPLASH sample can be further separated. Again using the PARSEC evolutionary tracks (Bressan et al. 2012), we were able to confirm that the dense clump of black points in the thin grey polygon on the UV/optical CMD (Fig. 1(b)) are BHeB stars. As can be seen in the histogram in Fig. 3, the blue stars in the SPLASH sample separate in to two groups, MS and BHeB stars (solid black Gaussian curves). As can be seen from the UV/optical CMD, there are Hα stars that lie outside the MS bin (dark blue), we therefore defined an additional polygon red-ward of the MS polygon by eye to enclose these additional Hα stars (pale blue). As can be seen from Fig. 3, this population of stars do not line up with either the MS or BHeB stars in colour space but instead falls between them (pale blue long-dash Gaussian). From this we conclude that these stars are 'transitioning' from the MS (T-MS) and not associated with the BHeB sequence. These T-MS stars are most likely stars that are evolving off the MS and their Hα emission is fading as a result. Alternatively, the T-MS stars could also be reddened MS stars. We classify 17 stars as T-MS Hα stars.

To investigate the properties of the T-MS stars, we wanted to define a 'normal' T-MS population. We therefore defined any SPLASH object that was enclosed in the T-MS bin but *not* in the BHeB bin as a 'normal' T-MS star. Taking a ratio of the Hα stars that fall in the 'normal' T-MS bin and the total number of SPLASH objects in the same region, we found a proportion of $\sim$ 5 per cent of the T-MS stars emit Hα.

4.1.4 Classifying RHeB Hα stars

For the redder stars in the SPLASH sample, we used the far-red/NIR (F814W/F110W) CMD in Fig. 1(c) to separate the different populations (Melbourne et al. 2012). We separated RHeB stars from AGB stars using the line defined by Rosenfield et al. (2016), and scaled to the TRGB in M31, shown by the dot-dash line. We defined RHeB Hα stars as those that lie red-ward of the optical $-$ far-red colour cut shown in Fig. 1(a) but blue-ward of the far-red $-$ NIR colour cut in Fig. 1(c). We classify 25 Hα stars as RHeB stars. As discussed in Rosenfield et al. (2016), this definition works best at brighter magnitudes but close to the TRGB, these populations become increasingly more merged. However, as we are unable to spectroscopically distinguish the RHeB stars from the AGB stars at this resolution (Melbourne et al. 2012; Dalcanton et al. 2012), we use this definition to separate RHeB stars from AGBs knowing that there could significant be contamination. Rosenfield et al. (2016) estimate the mean contamination by AGB stars in the RHeB population to be $\sim$ 4 per cent.

To define a 'normal' RHeB star population against which to compare the RHeB Hα stars, we again used the far-red/NIR CMD. We defined a polygon by eye that was positioned blue-ward of the Rosenfield et al. (2016) colour cut but above the TRGB (dense black points centred at F160W $\sim$ 19 mag). Comparing the RHeB Hα stars and the other SPLASH objects within this bin, we found a proportion of $\sim$ 4 per cent of RHeB stars emit Hα. To verify the RHeB Hα stars we defined that were not in the 'normal' RHeB bin were correctly classified, we inspected their individual spectra. While we were unable to definitively say whether a star was an AGB star or RHeB star, we could check that those outside the 'normal' RHeB bin had typical RHeB spectral features, i.e. strong TiO absorption. We found that stars

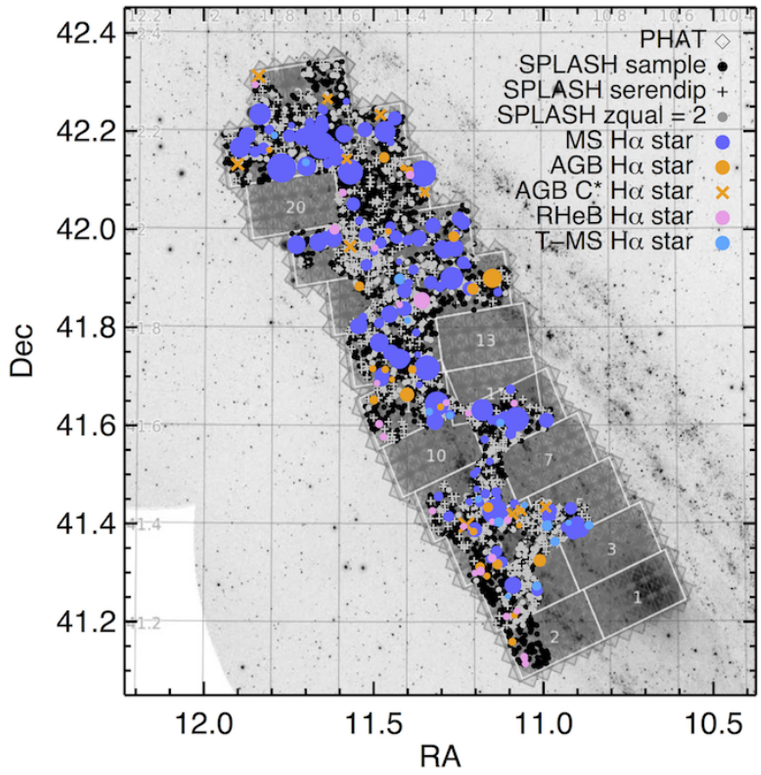

Figure 4. Spatial distribution of the spectroscopic and photometric samples in M31. The background is a composite of a GALEX image of M31 with the PHAT survey coverage shown by the grey 'bricks' (composed by Dustin Lang). Points follow the same labelling as Fig. 1. See §4.2.

blue-ward of the bin had TiO absorption and those below the bin, in the RGB clump, mostly had strong TiO absorption. The two with weaker TiO absorption that lie below the 'normal' RHeB bin, we have defined as 'RHeB?' in the Hα star catalogue in Appendix A but include in the RHeB class for the analysis.

4.1.5 Classifying AGB Hα stars

Following the classification of the RHeB stars from the AGB stars, we therefore defined all AGB stars as being those red-ward of the colour cut shown by the dot-dash line in Fig. 1(c) (orange points). The AGB Hα stars that lie below the TRGB are likely to be variable AGB stars at their minima, or contamination by symbiotic stars. We further separated the AGB stars in to non-C-rich (C/O $<$ 1) AGB stars and C-rich AGB stars (AGB C*) based on spectral features. The AGB C* Hα population is discussed in the next section. We found 25 non-C-rich AGB stars that emit Hα. To define a 'normal' AGB population we again drew a polygon by eye above the TRGB but extending red-ward of the RHeB/AGB colour cut (orange polygon). Using this reference sample and focusing just on the non-C-rich AGBs within the polygon, we found a proportion of $\sim$ 2 per cent emit Hα. As with the RHeBs, distinguishing AGBs from RHeBs can result in contamination. Rosenfield et al. (2016) determine the mean contamination by RHeBs in the AGB population to be $\sim$ 3 per cent.

4.1.6 Classifying AGB C Hα stars*

Those AGB Hα stars that are also C stars, as identified by Hamren et al. (2015), see §2.2, are shown by the orange X symbols in Fig. 1. We found 11 AGB C* Hα stars. From the total 5295 SPLASH spectra, we take all C stars red-ward of the RHeB/AGB colour cut (77 in total) to be our 'normal' AGB C* population. We conclude that $\sim$ 14 per cent of the C stars show Hα emission.

4.2 Spatial distribution

A 2D projection of the sample in M31 is shown in Fig. 4. The sample is plotted over a GALEX image of M31 with the PHAT survey coverage shown by the numbered grey 'bricks' (image by Dustin Lang). The spectroscopic sample lies within the region covered by the PHAT survey as a requirement of the SPLASH target selection. The points again follow the labelling convention of the CMDs in Fig. 1, where the small points indicate the total SPLASH sample of 5295, 600 line mm^{-1} spectra, and are split in to sub-categories. The larger points are the Hα stars separated in to five classifications; MS (dark blue points), T-MS (pale blue points), RHeB (pink points), AGB (orange points), and AGB C* (orange Xs). Their symbol size is a measure of their Hα emission-line strength (|EW|).

The richest sections of M31 covered by the PHAT survey were targeted by SPLASH in order to maximise the use of the DEIMOS masks. Therefore, the dense star forming rings were prioritised. To better understand the spa-

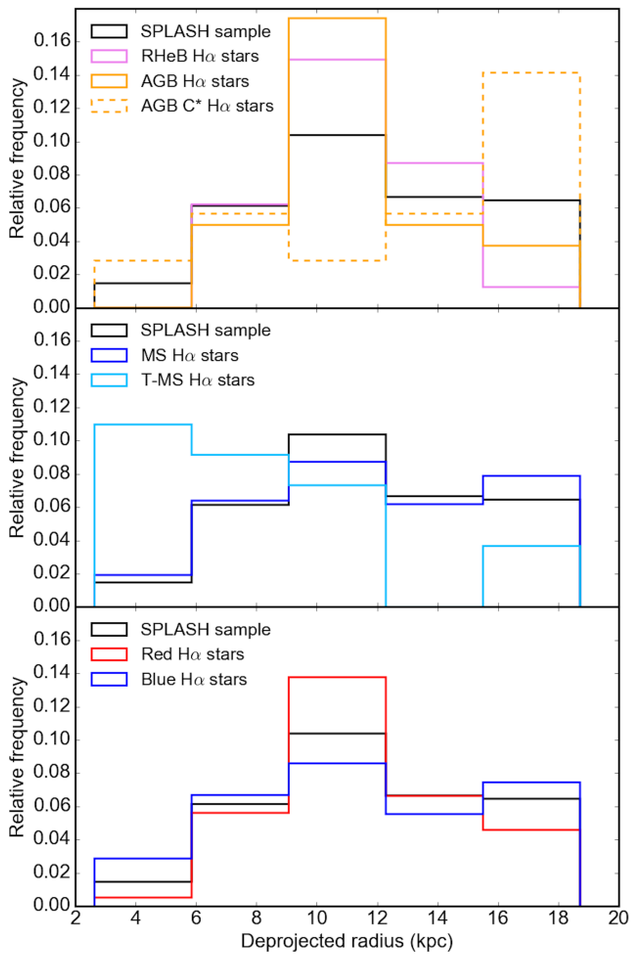

Figure 5. Histograms of the relative frequencies of the SPLASH sample (black) and Hα stars vs. R_{deproj}. Top panel shows red Hα stars. Middle panel shows blue Hα stars. Bottom panel shows the combined red and blue Hα stars. See §4.2.

tial distribution of the sample, we determined deprojected radii from the centre of M31 (R_{deproj}) of the stars. We used inclination angle $i = 70°$, position angle 43°, and centre $\alpha(2000) = 10.^{\circ}68473$ and $\delta(2000) = 41.^{\circ}26905$ (Dalcanton et al. 2012) to calculate R_{deproj}. The main features seen in this northeast quadrant of M31 are the 5-, 10-, and 15-kpc star forming rings (Lewis et al. 2015). These three main features, which are covered by the SPLASH survey, are at approximately $\alpha(2000) = 11.^{\circ}1$ and $\delta(2000) = 41.^{\circ}6$, $\alpha(2000) = 11.^{\circ}3$ and $\delta(2000) = 41.^{\circ}9$, and $\alpha(2000) = 11.^{\circ}7$ and $\delta(2000) = 42.^{\circ}2$ respectively on the 2D projection in Fig. 4. Given the targeted selection the SPLASH sample, we therefore look at the distribution of Hα stars relative to the total 600 line mm^{-1} SPLASH sample of 5295 objects, which peaks at the 10-kpc ring.

Histograms of the different types of Hα star as a function R_{deproj} are shown in Fig. 5. When splitting the red (all AGBs and RHeBs) from the blue stars (MS and T-MS) in the sample (bottom panel of Fig. 5), we find a relative increase in the number of red Hα stars in the 10-kpc ring. This is consistent with the prolonged star formation (SF), spanning ∼ 0.5–1 Gyrs, predicted to have occurred in this long-lived feature (e.g. Dalcanton et al. 2012; Lewis et al. 2015). The blue Hα stars seem to show a relative increase compared to the SPLASH sample at the inner and outer most regions, consistent with the 5-kpc ring 15-kpc ring respectively. It has been shown the 15-kpc ring has had a relatively recent SF burst, starting ∼ 80 Myrs ago (Lewis et al. 2015), consistent with the increased number of younger Hα stars.

Due to the small numbers of individual Hα star within their classes, excluding MS stars, it is difficult to describe trends in their distribution with certainty. In the middle panel of Fig. 5, we do see that the majority of the T-MS stars lie at $R_{deproj} < 12$ kpc. This could be due to more evolved MS stars existing in this region, consistent with slower and more extended SF (Lewis et al. 2015), but could also relate to increased dust that reddens the MS stars. As shown in the top panel of Fig. 5, the AGB and RHeB stars have a similar distribution across M31 with the relative peak in the 10-kpc ring appearing in both classes. As the AGB C*s are the smallest sub-group of Hα stars, drawing conclusions on their distribution is done so with caution. There appears to be a relative increase in the number of AGB C* Hα stars around the 15-kpc ring, as compared to the total number of SPLASH objects. As there is thought to have been a relatively recent SF burst, the presence of this older population of lower mass stars is less consistent. However, when looking at the AGB C* distribution in the 2D projection (Fig. 4), the AGB C*s are evenly spread throughout the outer region. This could mean these are halo stars projected onto the disc, or they could be the remnants of an older and more sparse population formed over a longer period of more quiescent SF, still in agreement with SF history (SFH) maps of the PHAT sample (Lewis et al. 2015).

4.3 Composite spectra

To inspect the spectral qualities of the five Hα star classifications we identified, we made composite spectra (i.e. mean spectra) of all those we selected in each group. The composite spectra shown in Figs. 6 to 10 are normalised to the continuum local to the Hα emission line and smoothed by 10 pixels. We identify the Hα emission line (dotted line) and show the broad telluric absorption features (magenta bands). For the SPLASH spectra, beyond the telluric feature at ∼ 9300 Å the spectrum is contaminated by 2nd order effects but we do not use any of this region in our analysis.

A composite spectrum of all the 146 MS Hα stars is shown in Fig. 6. The prominent Hα emission line at 6563 Å, shown by the dotted line, is the strongest spectral feature. The continuum is relatively smooth with broad sky absorption and some bad sky subtraction features. The composite spectrum of the 17 T-MS Hα stars in Fig. 7 has many similar properties to the MS stars. It has a slightly bumpier continuum but this could well be an effect of the small numbers of T-MS stars. However, the Hα line is noticeably weaker in the T-MS stars.

The composite spectrum for the 25 RHeB Hα stars is shown in Fig. 8 and for the 25 non-C-rich AGB is in Fig. 9. Despite their different evolutionary paths, these stars share similar properties and at the resolution of the SPLASH sample, cannot be spectroscopically distinguished (Melbourne et al. 2012; Dalcanton et al. 2012). The spectra of RHeB

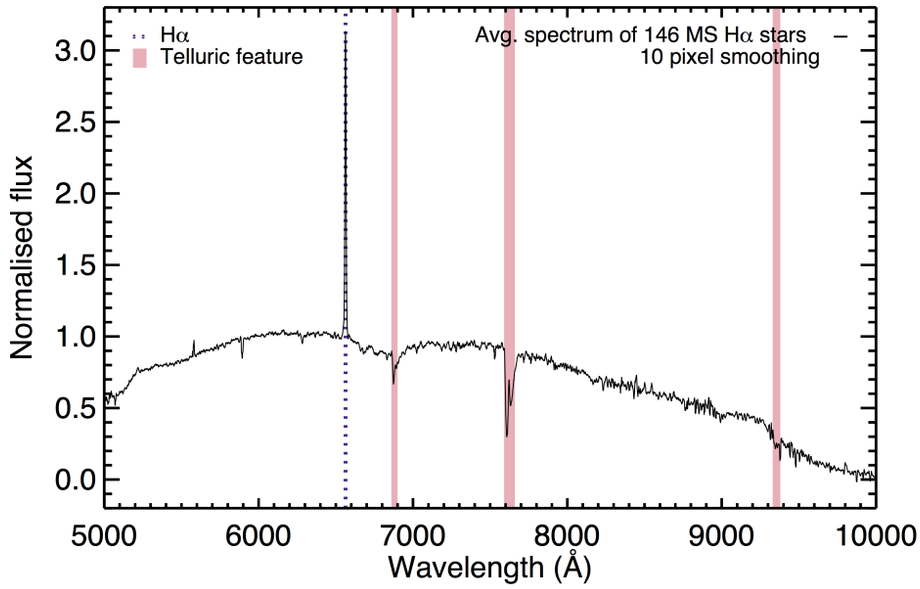

Figure 6. Composite spectrum of the 146 bright MS Hα stars, with 10-pixel smoothing. The continuum, normalised to the Hα region, is relatively smooth with emission and absorption lines. The Hα emission line (vertical dotted line) is prominent, there is broad telluric absorption lines at $\sim$ 6880 Å and $\sim$ 7620 Å shown by the magenta bands, and there is some bad sky subtraction seen in the spectrum.

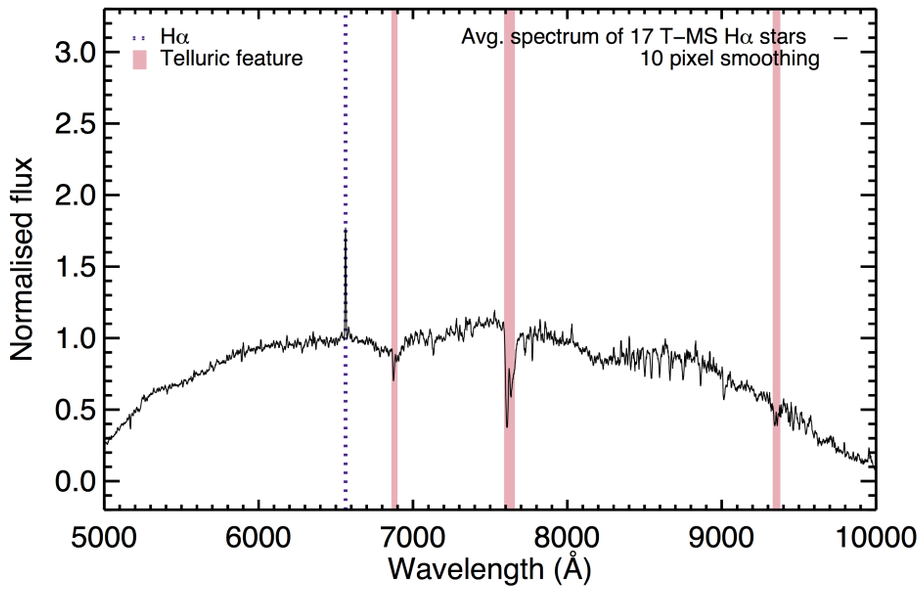

Figure 7. Composite spectrum of the 17 T-MS Hα stars, normalised to the Hα region, and with 10-pixel smoothing. The Hα emission line (vertical dotted line) and telluric absorption (magenta bands) are shown. The T-MS stars have similar spectral properties to the MS star spectrum in Fig. 6. However, they seem to show weaker Hα emission and have a bumpier continuum.

and AGB stars show strong TiO absorption features (faint bands). A composite spectrum of the 11 AGB C* Hα stars is shown in Fig. 10. Two carbon features are present in the spectrum; C_2 at $\sim$ 6100–6600 Å, and CN at $\sim$ 7900–8200 Å, shown by the darker bands.

4.4 Hα EW and velocity dispersion distribution

To investigate the physical properties of our sample of Hα stars from their spectra, velocity dispersion (σ_v) values were calculated from the width of the Hα emission line. The width of the Hα lines were calculated from the double Gaussian fit described in §3.2. The σ_v of the Hα line was then calculated by

$$\sigma_v = \left(\frac{\sigma_{H\alpha}}{\lambda_{H\alpha}}\right) \cdot c. \quad (4)$$

Here, $\sigma_{H\alpha}$ is the Hα line width, given by the STDEV from MPFITFUN, $\lambda_{H\alpha}$ is the wavelength of the Hα line, and c is the speed of light. The width of the emission line is a mea-

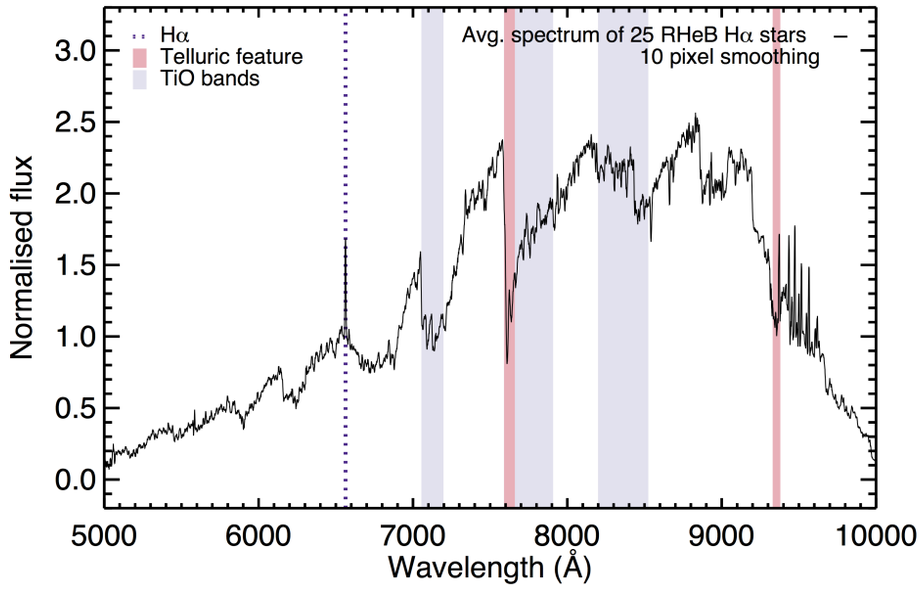

Figure 8. Composite spectrum of the 25 RHeB Hα stars, with continuum normalised to the Hα region and 10-pixel smoothing. The Hα emission line (vertical dotted line) and telluric absorption (magenta bands) are shown. The RHeB spectrum also shows strong TiO absorption features as indicated by the pale bands.

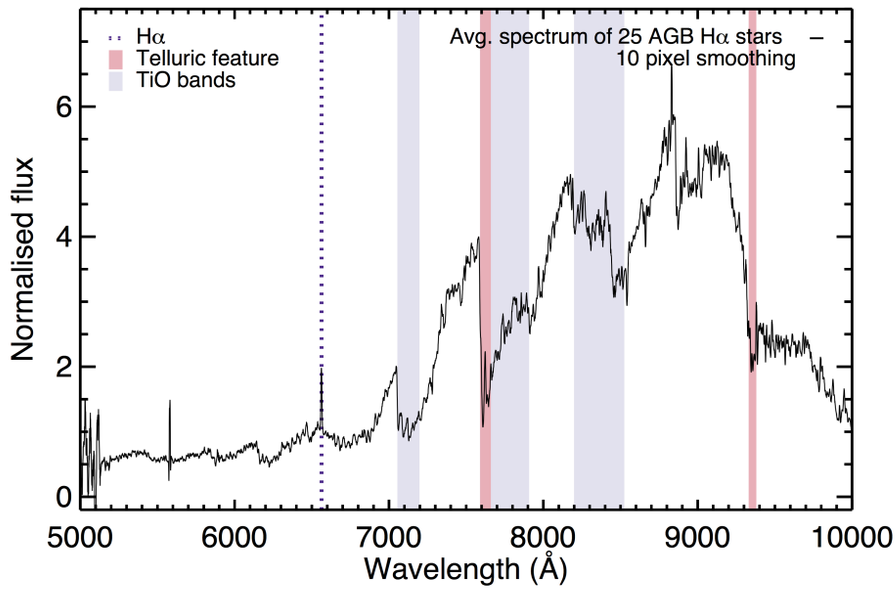

Figure 9. Composite spectrum of the 25 non-C-rich AGB stars with Hα emission, normalised to the Hα region continuum, and with 10-pixel smoothing. The Hα emission line (vertical dotted line), telluric absorption (magenta bands), and TiO absorption (pale bands) are shown. The AGB composite spectrum is very similar to the RHeB spectrum (Fig. 8) despite their different evolutionary paths.

sure of the Doppler broadening that occurs when moving material emits photons, i.e. a stellar wind or the pulsating outer layers of a star. Line broadening also depends on the spectral resolution of the instrument used for observations.

The distribution of σ_vs and EWs for the different classes of Hα stars is shown in Fig. 11. Fig. 11(a) shows MS (dark blue) and T-MS (pale blue) Hα stars, and the RHeB (pink points), AGB (orange points), and AGB C* (orange crosses) Hα stars are shown in Fig. 11(b). In both panels, the shaded region represents the approximate limit of Keck II/DEIMOS resolution. This value, around ~ 60 km s^{-1}, can vary, hence why the σ_v for some stars is below this limit, while the majority in this shaded region are unresolved. However, in this shaded region, the EW and thus the Hα detection is unaffected. In both plots, the horizontal and vertical dashed lines represent the median values of EW and σ_v respectively for each class of Hα star. A summary of these median values is given in Table 1 along with additional average values of each class.

The MS stars show a relatively broad range of σ_v values

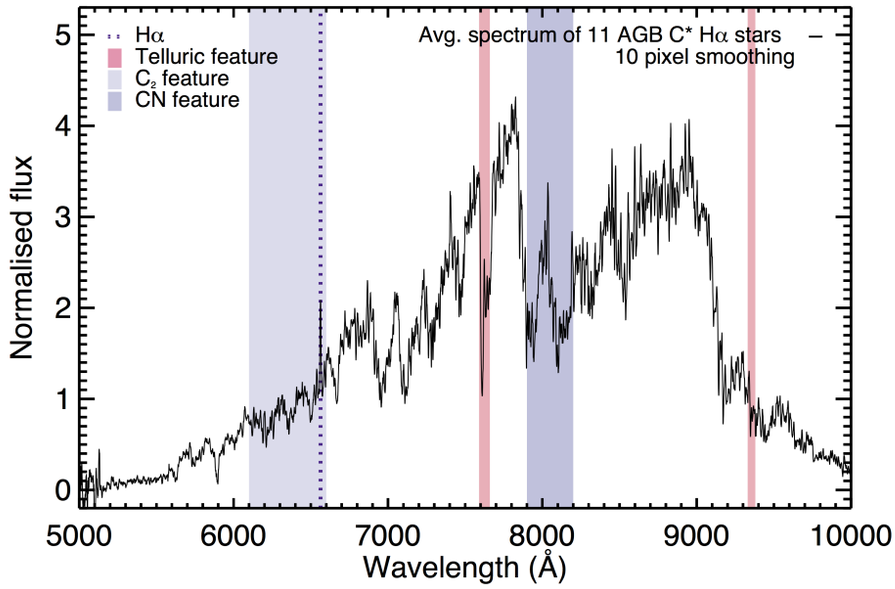

Figure 10. Composite spectrum of the 11 C-rich AGB stars with Hα emission, normalised to the Hα region, and with 10-pixel smoothing. The Hα emission line (vertical dotted line) and telluric absorption (magenta bands) are shown. The darker bands show the C_2 ($\sim$ 6100–6600 Å) and CN ($\sim$ 7900–8200 Å) features.

Table 1. Summary of properties and median values for the five classifications of Hα stars in our catalogue: MS, T-MS, RHeB, non-C-rich (C/O $<$ 1), and C-rich (C/O $>$ 1) AGB stars. The rows contain: number of Hα stars, proportion of their classification to emit Hα, median Hα EW and σ_v values, median magnitudes in the six HST filters (where data exists) and errors.

Classification	MS	T-MS	RHeB	AGB	
				C/O $<$ 1	C/O $>$ 1
Number	146	17	25	25	11
Proportion	$\sim$ 12%	$\sim$ 5%	$\sim$ 4%	$\sim$ 2%	$\sim$ 14%
Hα EW (Å)	-14.4 ± 1.1	-5.2 ± 0.9	-3.8 ± 1.0	-6.2 ± 1.5	-3.6 ± 1.3
Hα σ_v (km s^{-1})	112 ± 5	74 ± 11	55 ± 5	65 ± 9	59 ± 12
F275W (mag)	20.4 ± 0.1	22.3 ± 4.6	-	-	-
F336W (mag)	20.4 ± 0.6	21.3 ± 0.3	27.6 ± 6.4	28.6 ± 7.1	-
F475W (mag)	21.6 ± 0.1	21.4 ± 0.3	23.1 ± 0.2	25.4 ± 0.3	24.5 ± 0.3
F814W (mag)	21.3 ± 0.1	20.8 ± 0.3	20.0 ± 0.2	20.7 ± 0.1	19.8 ± 0.2
F110W (mag)	21.3 ± 0.1	20.6 ± 0.3	19.3 ± 3.2	18.9 ± 0.2	18.5 ± 0.2
F160W (mag)	21.1 ± 0.5	20.2 ± 0.3	18.6 ± 3.3	18.0 ± 0.2	17.3 ± 0.2

that go up to $\sim$ 300 km s^{-1}, with a median of 112 ± 5 km s^{-1} (dark blue dashed vertical line). The MS Hα stars show a large spread of EW values going up to ~ -60 Å. The median value of the MS Hα star EW (dark blue dashed horizontal line) is $\sim -14.4 \pm 1.1$ Å. The T-MS Hα stars occupy a much smaller region of the plot with lower median σ_v values (pale blue dashed vertical line) of 74 ± 11 km s^{-1} and median EW $\sim -5.2 \pm 0.9$ Å (horizontal line). As could also be seen from the composite spectrum in Fig. 7, the T-MS Hα stars show weaker emission.

In Fig. 11(b) the AGB stars show the largest spread of EWs and σ_v values. The red Hα stars have similar median σ_v values (vertical lines); RHeBs at 55 ± 5 km s^{-1} (pink dashed line), AGBs at 65 ± 9 km s^{-1} (orange dashed line), and AGB C*s at 59 ± 12 km s^{-1} (orange dotted line). However, all of these median σ_v values are on the cusp of the approximate limit of Keck II/DEIMOS resolution and so are mostly unresolved. The non-C-rich AGB stars have a larger median |EW| value of $\sim -6.2 \pm 1.5$ Å (orange dashed horizontal line). The RHeBs and AGB C*s both have similar and weaker median Hα emission at $\sim -3.8 \pm 1.0$ Å and $\sim -3.6 \pm 1.3$ Å respectively.

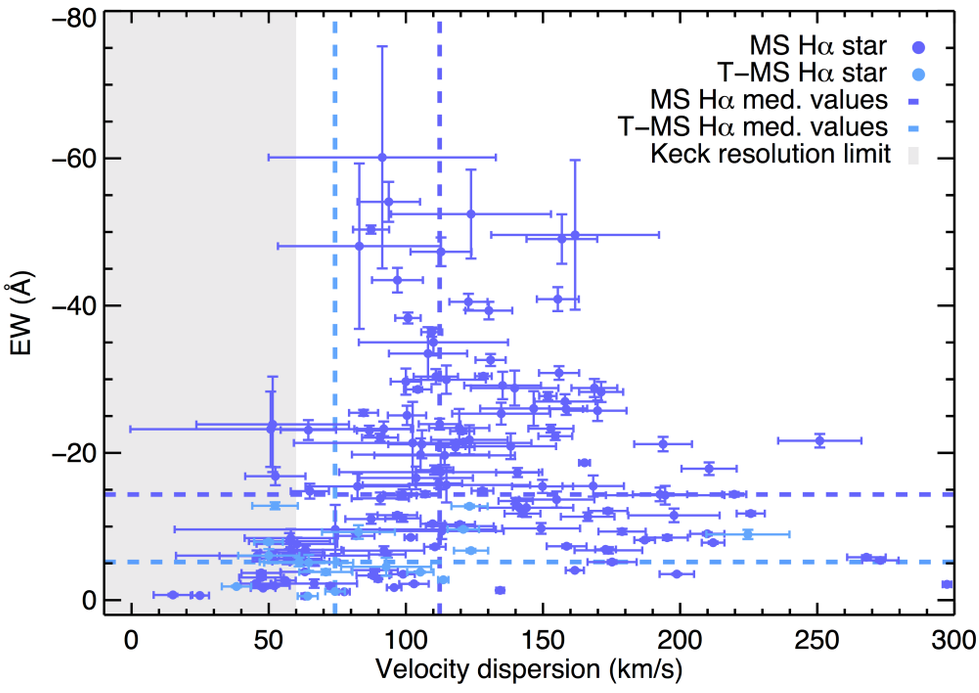

(a)

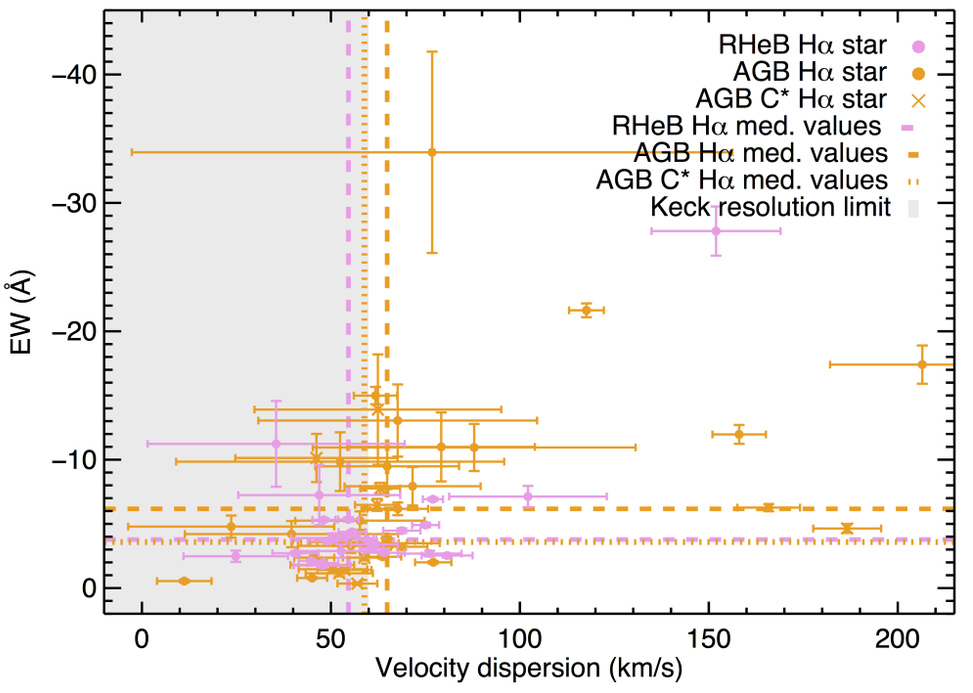

(b)

Figure 11. Hα line strength (EW) vs. σ_v of Hα stars. Shaded region in both panels is approximate spectral resolution limit for Keck II/DEIMOS ($\sim$ 60 km s^{-1}), however this can vary so some σ_v values below this limit are resolved. Median EW and velocity values for the Hα stars are indicated by the dashed horizontal and vertical lines respectively. (a) MS Hα stars (dark blue) and T-MS Hα stars (pale blue). (b) RHeB Hα stars (pink), non-C-rich AGB Hα stars (orange points), and C-rich AGB Hα stars (orange Xs). The majority of these stars have σ_v values that are unresolved. See §4.4 and Table 1.

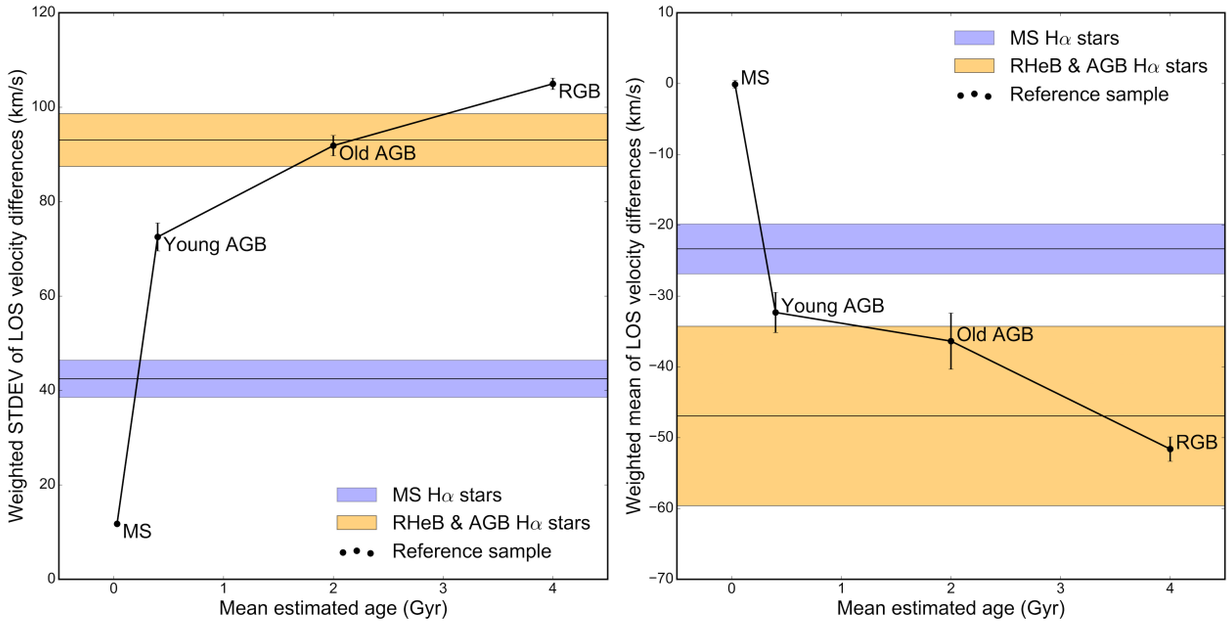

(a) (b)

Figure 12. (a) LOSVD vs. mean estimated age for reference sample of normal MS, bright/young AGB, faint/old AGB, and RGB stars (black points) and MS Hα stars (blue band), and RHeB and AGB Hα stars (orange band). LOSVD calculated as the weighted STDEV of LOS velocity differences and is an indicator of age. (b) Same as left panel, except y-axis is the weighted mean (rather than weighted STDEV) of the LOS velocity differences. Similar trends are observed. See §4.5.

4.5 Hα star kinematics

A recent study using the SPLASH and PHAT samples investigated the line-of-sight stellar velocity dispersion (LOSVD) of stars in M31 as a function of their age and metallicity (Dorman et al. 2015). Splitting stellar populations in to four categories based on their position in the optical PHAT CMD, they then calculated the ages of these populations based on simulated CMDs. The four categories were young MS, bright/young AGB, faint/old AGB, and RGB stars, with mean ages were 30 Myrs, 0.2 Gyrs, 0.4 Gyrs, and 2 Gyrs respectively. The LOSVD for each of the four age bins was determined by measuring the dispersion of each population within radial bins (of 200″ up to 275″). Stars with less than 15 neighbours within the radial bin were dropped from the analysis as their calculated LOSVD and error were deemed unreliable. They found that the older populations were dynamically hotter than the younger populations, ranging from 30 km s^{-1} for MS stars to 90 km s^{-1} for RGB stars outward from $R_{deproj} \sim 10$ kpc. This linear increase in LOSVD indicated a continuous or recurring process contributed to the evolution of the disc, whereby the older populations have had more time to be perturbed from their original velocity.

We used a modified version of the kinematic analysis method done by Dorman et al. (2015) in order to predict the ages of the Hα MS (not including the T-MS) stars and the red Hα stars. Fig. 12 shows the reference SPLASH sample separated in to the four age bins (black points), and the MS and red Hα stars represented by the horizontal blue and orange bands respectively. Here we have combined the RHeBs, AGBs, and AGB C*s in to the red stars category due to their limited numbers, we do note that this will then increase the error margins on the calculated ages. Because Hα stars are relatively sparse, the LOSVDs were calculated as LOS velocity differences between the weighted mean of MS star neighbours (within r < 275″) and the LOS velocity of the Hα stars, instead of the weighted STDEV of Hα neighbours. The MS population is used to define the velocity reference frame because it is the most well-ordered (dynamically cold) of M31's stellar populations. The mean was weighted inversely proportional to the square of the velocity measurement errors. LOSVDs were calculated for MS, bright/young AGB, faint/old AGB, and RGB age bins using the reference SPLASH sample. In accordance with the results from Dorman et al. (2015), LOSVD increased with the age of the stellar population. Hα MS stars (blue bands) had LOSVDs similar to bright/young AGB stars, and the redder Hα stars (RHeBs, AGBs, and AGB C*s; orange bands) had LOSVDs similar to faint/old AGB stars. The ages of Hα stars appear to correspond with that of their non-emission counterparts.

4.6 Be/(Be + B) variations

Studies of the ratio of Be stars to all B stars (Be/(Be + B)) have shown it is dependent on ages of stars (Fabregat & Torrejón 2000) and the metallicity of their environment (Maeder, Grebel & Mermilliod 1999; Martayan et al. 2007). Due to the size of the sample of MS Hα stars we have selected, the range of different environments, and spatial extent covered by the data sets, we were able to investigate how this ratio changes in M31. Fig. 13 shows histograms of the relative frequencies of Be stars and all B stars, and how their ratio varies as a function of F336W magnitude and R_{deproj}.

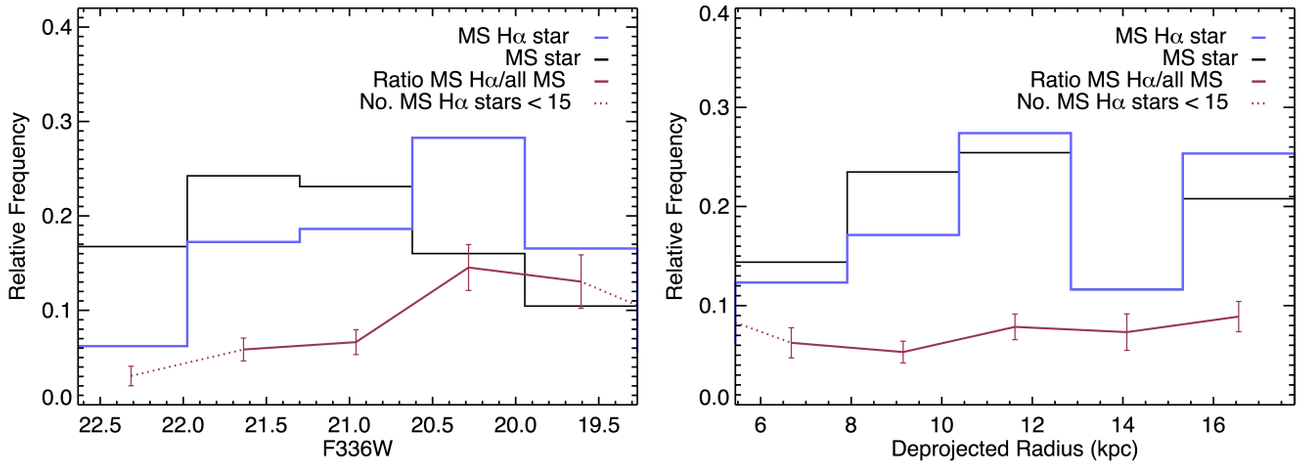

(a) (b)

Figure 13. Histograms of the MS Hα stars (blue) to all MS stars (black) ratio (i.e. Be/(Be + B)) as a function of F336W magnitude (a) and R_{deproj} (b). Ratio of the two shown by the red line. Bins with > 15 MS Hα stars are shown by the solid red line. Values of the Be/(Be + B) ratio are given for these bins in Table 2. See §4.6.

Table 2. Be/(Be + B) values at different values of F336W magnitude and R_{deproj} (see Fig. 13). Shown in the table are only those bins that contain > 15 Hα stars, ∼ 10 per cent of the MS Hα sample.

Varied Quantity		Be/(B + B)		
F336W	21.6	6%	±	1%
	21.0	7%	±	1%
	20.3	15%	±	2%
	19.6	13%	±	3%
Deprojected Radius (kpc)	6.7	6%	±	2%
	9.1	5%	±	1%
	11.6	8%	±	1%
	14.1	7%	±	2%
	16.6	9%	±	2%

The solid line red line shows how the Be/(Be + B) ratio varies as a function of the x-axis for bins with > 15 (∼ 10 per cent of all MS Hα stars) Be stars in a bin. The values of the Be/(Be + B) ratio for these different histograms are given for all those bins with > 15 Be stars in Table 2.

Fig. 13(a) shows how the Be/(Be + B) ratio varies with F336W magnitude, which can also be interpreted as stellar mass but that also has a metallicity dependence. The ratio significantly increases between the second and third bin (∼ 21.0–20.3 mag). This could be a metallicity dependence on the ratio, as seen in other studies, or a dependence of this ratio on stellar mass, i.e. higher mass MS stars are more likely to emit Hα.

To investigate the dependence of the Be/(Be + B) ratio on environment, we investigate how it varies as a function of R_{deproj} from the centre of M31, which spans a variety of different metallicity regions. Although there is no obvious overall trend of the ratio with radius, there is a slight increase of the ratio at larger radii than the centre. This would follow the metallicity gradient of M31 (e.g. Zurita & Bresolin 2012; Gregersen et al. 2015), as the Be/(Be + B) fraction is higher in lower metallicity environments.

5 DISCUSSION

The PHAT and SPLASH data show the Hα stars fall in to five classes: bright MS, T-MS, RHeB, AGB, and AGB C* stars. Despite the fact that these stars all exhibit Hα emission, their evolution, properties, and mechanisms of emission are very different. In this section we will discuss the five classifications of Hα stars separately in §5.1 to §5.5 respectively.

5.1 MS Hα stars

Of the bright MS stars in the sample, ∼ 12 per cent of them were classified as Hα stars. Due to the rarity of O-type stars, we assume that the MS part of the sample contains solely B-type stars for simplicity. Looking at the spatial distribution of the Be stars, we found that there was a relative increase in their number compared to the SPLASH sample at R_{deproj} of ∼ 15 kpc (see Figs. 4 and 5). This presence of these young massive stars is consistent with the 15-kpc star forming ring of M31 that was found to have had a relatively recent SF burst, starting ∼ 80 Myrs ago (Lewis et al. 2015).

Due to the metallicity dependence of the Be/(Be + B) ratio, a previous study investigated a range of environments in the LG with different metallicities. Be/(Be + B) ratios of 11, 19, 23, and 39 per cent were determined for star clusters that decreased in metallicity, in the inner and outer Galaxy, LMC and SMC respectively. The 'inner MW' was defined as star clusters at galactocentric radii of < 8 kpc and 'outer MW' as > 8 kpc (Maeder, Grebel & Mermilliod 1999). We found an average Be/(Be + B) proportion of ∼ 12 per cent in M31, i.e. both disc and halo stars, out to R_{deproj} ∼ 20 kpc from the centre of M31. To ensure that we were comparing the samples accurately, we compared the

absolute magnitude range used by Maeder, Grebel & Mermilliod (1999) to our sample, and we found that we were probing the same stellar population at the distance of M31. This average value for Be/(Be + B) in the inner and outer regions of M31 is consistent with the $\sim$ 11 per cent found in just the metal-rich inner region of the MW. When looking at the histogram in Fig. 13(b), and the values in Table 2 for the bins with $>$ 15 MS Hα stars, the values range from 6 $\pm$ 2 per cent to 9 $\pm$ 2 per cent, for R_{deproj} of 6.7 and 16.6 kpc respectively. The average of these values between those radii would give a Be/(Be + B) ratio of 7 $\pm$ 2 per cent. This ratio of Be/(Be + B) stars in M31 could indicate that it has a higher metallicity than the MW. This would agree with other studies that suggest M31 is likely to be more metal rich than the MW, and may have had a more recent and active accretion history of satellites galaxies (e.g. Kalirai et al. 2006; Brown et al. 2006). A more turbulent evolution could have catalysed more star formation in M31, increasing its overall metallicity.

Given the diverse range of environments our Be sample spans in M31, these stars are ideal candidates for follow up observations. Monitoring the variability of the Hα emission seen in these stars across these environments will allow us to better understand its nature. Cross matching the sample of Be and B stars to the SFH maps from Lewis et al. (2015), and metallicity maps of M31, may break the degeneracy in the age-metallicity dependence of the Be phase.

5.2 T-MS Hα stars

We identified T-MS Hα stars as those not within the MS stellar bin on the UV/optical CMD in Fig. 1(b) but not associated with the BHeB phase of evolution as shown by the histogram in Fig. 3. We found 17 T-MS Hα stars, and show that this makes up $\sim$ 5 per cent of this 'transitioning' population. It is likely that these are Be stars evolving off the MS. High mass MS stars evolve rapidly after H burning due to the quick contraction in the core and expansion in the envelope. Stars can traverse the CMD from MS to massive red stars in $\sim$ 1 Myr (Hayashi, Nishida & Sugimoto 1962), hence why the T-MS bin is sparsely populated. Their expansion causes the rotation of their envelope to slow as they conserve angular momentum. As the Be stars could emit Hα via a rotationally flattened disc (e.g. Struve 1931; Dougherty & Taylor 1992), if stellar rotation slows, the Hα emission from this circumstellar disc would fade as a star evolves off the MS. However, these stars could also be reddened MS Hα stars that appear to have left the MS in UV/optical colour space.

As seen in our sample of Hα stars, these T-MS stars have characteristically weaker Hα emission as shown by their composite spectra (Fig. 7), distribution of EW values (Fig. 11(a)), and median population values of EW and σ_v (Table 1), as compared with the MS Hα stars. Being cautious not to draw any strong conclusions from their spatial distribution due to their small number, we do see that the majority of T-MS stars lie within R_{deproj} = 12 kpc (Figs. 4 and 5). The presence of these perhaps older more evolved MS stars is then consistent with the prolonged SF in this region (Dalcanton et al. 2012; Lewis et al. 2015), but could also be more reddened by an increase in the dust within this region. Given our multi-faceted data set, separating the MS and BHeB stars was possible in the UV/optical CMD (Dohm-Palmer et al. 1997; Dohm-Palmer & Skillman 2002), and the Keck/II DEIMOS spectra allowed us to resolve Hα emission for these stars in M31. As a result of combining the PHAT and SPLASH data we have been able to identify this population but do not have many comparative samples against which to compare our T-MS Hα stars. However, for the first time we may have captured the evolution of Be stars off the MS as they traverse the CMD towards the RHeB sequence.

5.3 RHeB Hα stars

We separated the RHeB stars from the AGB stars in our sample using the far-red/NIR CMD (Melbourne et al. 2012), and using the colour cut defined by Rosenfield et al. (2016). The stars we identified as RHeB Hα stars are likely to be RHeB stars that are evolving up their Hayashi lines and becoming AGB stars. Compared to their 'normal' population, we found $\sim$ 4 per cent of the RHeB stars show Hα emission. The Hα emission we detect in the RHeB stars is weaker than those of the AGB stars, as can be seen by their distribution of EW values (Fig. 11(b)), and corresponding median population values (Table 1). As seen in Figs. 4 and 5, the RHeB stars show a relative increase in their numbers as compared to the total SPLASH sample at the 10-kpc star forming ring of M31. This increase in these older stars support the prolonged SF activity, up to 1 Gyr, in the 10-kpc ring (Dalcanton et al. 2012; Lewis et al. 2015). It is likely that many RHeB stars are misclassified as AGB stars in other studies without the far-red/NIR CMD to separate them. However, given the fact that these stars both show emission of Hα and that at this evolutionary stage, the lower- and higher-mass stars go through qualitatively similar evolution, we predict that these RHeB stars with Hα emission also fall under the LPV classification, and are either SRs or Miras.

There has been some discrepancy in the literature over what the ratio of BHeB to RHeB stars should be, and what is observed (e.g. Gallart, Zoccali & Aparicio 2005, and references therein). The number of BHeB stars we found in our sample, as defined in the thin grey polygon in Fig. 1(b) is $\sim$ 640. By accounting for the density of the 'normal' T-MS stars that could be crossing the BHeB sequence, we estimate the total number of BHeBs to be $\sim$ 500. The number of RHeB stars in the 'normal' RHeB bin defined in Fig. 1(c) is $\sim$ 360. As we know from CMD space and evolutionary tracks, RHeB stars exist outside of our defined 'normal' polygon but we avoided the RGB stars to reduce contamination. Using the ratio of RHeB Hα stars within and outside of the RHeB bin, we predict there are $\sim$ 560 RHeB stars in total. These numbers are crude approximations but we do find there are similar numbers of RHeBs to BHeBs as is also seen in other studies (McQuinn et al. 2011; Melbourne et al. 2012).

5.4 AGB Hα stars

Only $\sim$ 2 per cent of the non-C-rich AGB stars in the SPLASH sample exhibit Hα emission. Due to their characteristic Balmer emission, the AGB Hα stars in the sample are likely to be LPVs, either SRs or Miras. Given that we do

not have K-band, multi-epoch observations, we are unable to distinguish between Miras and SRs in our selected Hα sample (e.g. Battinelli & Demers 2014). Of the two broad LPV categories, Miras are more useful for studying stellar populations and galactic properties. Due to their period-luminosity relationship (e.g. Glass & Evans 1981; Glass & Feast 1982), they can be used as standard candles for intermediate age stellar populations (Whitelock 2012). Identifying them in M31 and improving our understanding of this evolutionary stage will help to refine their use as standard candles, and ultimately improve distance measurements to M31 and other systems. For old to intermediate age populations that lack younger stars, where distance indicators such as Cepheid variables are rare, Mira variables are good alternative standard candles. The selected AGB Hα stars are ideal for follow-up observations due to their number and shared environment.

AGB and RHeB stars trace a similar spatial distribution in M31, also exhibiting a relative increase in frequency at the 10-kpc ring (Figs. 4 and 5), consistent with prolonged SF activity in this region (Dalcanton et al. 2012; Lewis et al. 2015). Stars in the mass range $\sim$ 0.8 to 8 $M_{\odot}$ have qualitatively similar evolutionary paths when burning He/H in their shells and with a degenerate C-O core. We therefore conclude that the Hα emission in both the RHeB population (25 stars) and the stars firmly on the AGB (36 stars, including AGB C*s) are all LPVs. The sample of up to 61 potential Mira variables we have found, is the largest spectroscopically discovered sample of LPVs in M31.

5.5 AGB C* Hα stars

A recent study investigating the C-Mira/C star proportion in systems of a range of masses and metallicities around the LG had a consistent value of $\sim$ 12 per cent (Battinelli & Demers 2014). However, a C-Mira/C star value of up to 50 per cent was found in the MW halo and Sgr dSph (Battinelli & Demers 2014, 2013). Of the 77 C stars found in the 600 line mm^{-1} SPLASH spectra (Hamren et al. 2015, see §2.2) and red-ward of the colour cut shown in Fig. 1(c), 11 of these show Hα emission. This proportion of 14 per cent of AGB C*s in M31 exhibiting Hα emission is an upper limit to the C-Mira/C star ratio for M31. If there are SRs in our sample, this value will decrease. The upper limit fits with observations in other LG galaxies but differs significantly from the $\sim$ 40–50 per cent found in the MW halo and Sgr dSph (Mauron et al. 2014; Battinelli & Demers 2014, 2013, respectively). To ensure this was a fair comparison, we compared our NIR filter magnitudes, F110W (J-band equivalent) and F160W (H-band equivalent), and found that we are probing the same population of stars at the distance of M31 as observed in the MW halo. The cause of this disparity is most likely due to the different environmental effects of each sample. The properties of this population would be interesting to study further.

6 CONCLUSION

We identified and classified Hα stars in M31 using spectroscopy from Keck II/DEIMOS collected for the SPLASH survey and supporting six-filter photometry from HST collected as part of the PHAT survey. We devised a selection algorithm that implemented a set of six selection criteria to find a clean sample of Hα stars. From 5295 SPLASH spectra, we selected a sample of 224 Hα stars in M31. See Appendix A for a full list of selected Hα stars and their properties. We used a combination of CMDs and spectral features in order to classify the Hα stars. We have identified five classifications of Hα stars; MS, T-MS, RHeB, AGB, and AGB C* stars. The results from the analysis of these five categories of Hα star are summarised below.

- We found 146 MS Hα stars, meaning $\sim$ 12 per cent of the B-type MS stars were classified as Be stars. The proportion of Be/(Be + B) stars has been found to be dependent on the metallicity of their environment. When comparing our results with previous studies, the average proportion of Be to B stars that we found at a range of $R_{deproj} \sim 6$ to 16 kpc of 7 $\pm$ 2 per cent could indicate that M31 is more metal rich than the MW, supporting the findings of other studies.

- We defined a population of Hα stars red-ward of the MS on the UV/optical CMD as a T-MS population. These stars had characteristically weaker emission than the MS Hα stars, and were not associated with the BHeB star overdensity seen in the parent SPLASH sample. We concluded that these 17 T-MS Hα stars ($\sim$ 5 per cent of the 'normal' T-MS population), are Be stars evolving off the MS and their Hα emission fades as the star's outer layers expand and its rotation slows. This could be the first time the evolution of Be stars off the MS has been captured in CMD space. However, we note that these stars could also be reddened MS Hα stars.

- Using the far-red/NIR CMD, we were able to separate RHeB stars from AGB stars in our sample. There are approximately a similar number of BHeB to RHeB stars in the SPLASH sample. We found 25 of the RHeB stars showed Hα emission, $\sim$ 4 per cent of the RHeB population. Given the similarity in the evolutionary paths of stars in the mass range $\sim$ 0.8 to 8 $M_{\odot}$ beyond the HeB phase, we predict that these RHeB stars are evolving on to the AGB. Due to exhibiting Hα emission, we conclude that these stars, that are often misidentified as AGB stars, are undergoing regular dynamic pulsations in their outer layers causing the shock excited Balmer emission. We conclude that the RHeB Hα stars are LPVs, and are either Mira or SR variables.

- We found a sample of 25 non-C-rich AGB Hα stars, making up just $\sim$ 2 per cent of the non-C-rich AGB population. The presence of Hα emission in the AGB stars means that these stars are LPVs. Of these LPVs, the AGB Hα stars could be SRs or Miras. We found a relative excess of AGBs, and all other red stars in our sample as compared to the parent SPLASH sample, around the 10-kpc star forming ring in M31. This supports evidence from other studies of prolonged star formation in this long-lived feature.

- We found 11 AGB C* Hα stars, which is a proportion of $\sim$ 14 per cent of the C stars in the SPLASH sample that exhibit Hα emission, which is an upper limit for the C-Mira/C star ratio in M31. This is consistent with many other galaxies in the LG, although this value is likely to

be lower than this due to the presence of SRs. Regardless, this value differs significantly from the $\sim$ 40–50 per cent C-Mira/C star proportion in the MW halo and Sgr dSph, and this disparity is worth additional investigation.

• Combining the total number of RHeB, and AGB stars, both O and C rich, we found a sample of 61 LPV stars in our sample. This is the largest spectroscopically identified sample of LPVs in M31. This catalogue can be used to improve the use of Mira variables as distance indicators for intermediate-age populations of stars and the potential C-Miras can be used to investigate the properties of M31.

ACKNOWLEDGEMENTS

L.J.P. wishes to thank collaborators at the University of California Santa Cruz (UCSC) for use of their data and for their supervision, and thanks the University of Leeds for supporting the collaboration with UCSC for this project. L.J.P. also thanks collaborators at Leeds, UCSC, and Oxford for useful discussion and support. L.J.P is supported by a Hintze Scholarship, awarded by the Oxford Centre for Astrophysical Surveys, which is funded through generous support from the Hintze Family Charitable Foundation. L.J.P. acknowledges financial support from the Royal Astronomical Society Research and Grants Fund, supervisors at UCSC and University of Oxford, and Christ Church, Oxford. P.G., K.M.H., and C.E.D. were supported by NSF grant AST-1412648 and NASA/STScI grant HST-GO-12055. G.A.D., A.I., and M.I. carried out their work as part of the Science Internship Program at UCSC. We are grateful to the anonymous referee for useful comments that helped improve the clarity of the paper.

REFERENCES

Allen D. A., 1984, Proc. of the Astron. Soc. of Aus., 5, 369
Arndt T. U., Fleischer A. J., Sedlmayr E., 1997, A&A, 327, 614
Azzopardi M., Meyssonnier N., 1986, in IAU Symp., Vol. 116, Luminous Stars and Associations in Galaxies, De Loore C. W. H., Willis A. J., Laskarides P., eds., p. 225
Battinelli P., Demers S., 2005, A&A, 434, 657
Battinelli P., Demers S., 2013, A&A, 553, A93
Battinelli P., Demers S., 2014, A&A, 568, A100
Bertelli G., Bressan A., Chiosi C., Fagotto F., Nasi E., 1994, A&AS, 106
Blum R. D. et al., 2006, AJ, 132, 2034
Bohannan B., Epps H. W., 1974, A&AS, 18, 47
Bowen G. H., 1988, ApJ, 329, 299
Boyer M. L. et al., 2011, AJ, 142, 103
Bressan A., Marigo P., Girardi L., Salasnich B., Dal Cero C., Rubele S., Nanni A., 2012, MNRAS, 427, 127
Brown T. M., Smith E., Ferguson H. C., Rich R. M., Guhathakurta P., Renzini A., Sweigart A. V., Kimble R. A., 2006, ApJ, 652, 323
Cioni M.-R. L., Habing H. J., 2003, A&A, 402, 133
Cioni M.-R. L. et al., 2008, A&A, 487, 131
Cioni M.-R. L., Marquette J.-B., Loup C., Azzopardi M., Habing H. J., Lasserre T., Lesquoy E., 2001, A&A, 377, 945
Cooper M. C., Newman J. A., Davis M., Finkbeiner D. P., Gerke B. F., 2012, spec2d: DEEP2 DEIMOS Spectral Pipeline. Astrophysics Source Code Library
Dalcanton J. J. et al., 2012, ApJS, 200, 18
Dohm-Palmer R. C., Skillman E. D., 2002, AJ, 123, 1433
Dohm-Palmer R. C. et al., 1997, AJ, 114, 2527
Dorman C. E. et al., 2012, ApJ, 752, 147
Dorman C. E. et al., 2015, ApJ, 803, 24
Dougherty S. M., Taylor A. R., 1992, Nature, 359, 808
Downes R. A., Keyes C. D., 1988, AJ, 96, 777
Faber S. M., French H. B., 1980, ApJ, 235, 405
Fabregat J., Torrejón J. M., 2000, A&A, 357, 451
Feast M. W., 1996, MNRAS, 278, 11
Feast M. W., Abedigamba O. P., Whitelock P. A., 2010, MNRAS, 408, L76
Feast M. W., Glass I. S., Whitelock P. A., Catchpole R. M., 1989, MNRAS, 241, 375
Frogel J. A., Mould J., Blanco V. M., 1990, ApJ, 352, 96
Frogel J. A., Persson S. E., Cohen J. G., 1980, ApJ, 239, 495
Gallart C., Zoccali M., Aparicio A., 2005, ARA&A, 43, 387
Gehrz R., 1989, in IAU Symp., Vol. 135, Interstellar Dust, Allamandola L. J., Tielens A. G. G. M., eds., p. 445
Glass I. S., Evans T. L., 1981, Nature, 291, 303
Glass I. S., Feast M. W., 1982, MNRAS, 199, 245
Gregersen D. et al., 2015, AJ, 150, 189
Hamren K. M. et al., 2015, ApJ, 810, 60
Hayashi C., Hoshi R., 1961, PASJ, 13, 442
Hayashi C., Nishida M., Sugimoto D., 1962, Progress of Theoretical Physics, 27, 1233
Henize K. G., 1956, ApJS, 2, 315
Hughes S. M. G., 1989, AJ, 97, 1634
Hughes S. M. G., Wood P. R., 1990, AJ, 99, 784
Ibata R. A., Gilmore G., Irwin M. J., 1994, Nature, 370, 194
Iben, Jr. I., 1974, ARA&A, 12, 215
Iben, Jr. I., Renzini A., 1983, ARA&A, 21, 271
Jaschek M., Jaschek C., Hubert-Delplace A.-M., Hubert H., 1980, A&AS, 42, 103
Joy A. H., 1954, ApJS, 1, 39
Kalirai J. S. et al., 2006, ApJ, 648, 389
Karakas A. I., 2014, MNRAS, 445, 347
Karakas A. I., Lattanzio J. C., Pols O. R., 2002, PASA, 19, 515
Kerschbaum F., Hron J., 1992, A&A, 263, 97
Kun M., 1992, A&AS, 92, 875
Lewis A. R. et al., 2015, ApJ, 805, 183
Lloyd Evans T., Menzies J. W., 1973, in Astrophysics and Space Science Library, Vol. 36, IAU Colloq. 21: Variable Stars in Globular Clusters and in Related Systems, Fernie J. D., ed., p. 151
Maeder A., Grebel E. K., Mermilliod J.-C., 1999, A&A, 346, 459
Marigo P., 2002, A&A, 387, 507
Martayan C. et al., 2007, in SF2A-2007: Proc. of the Ann. meeting of the Fr. Soc. of Astron. and Astrophys., Bouvier J., Chalabaev A., Charbonnel C., eds., p. 512
Martayan C., Zorec J., Baade D., Frémat Y., Fabregat J., Ekström S., 2011, Bull. de la Soc. R. des Sci. de Liege, 80, 285
Massey P., Olsen K. A. G., Hodge P. W., Strong S. B., Jacoby G. H., Schlingman W., Smith R. C., 2006, AJ,

131, 2478
Mattsson L., Wahlin R., Höfner S., 2010, A&A, 509, A14
Mauron N., Gigoyan K. S., Berlioz-Arthaud P., Klotz A., 2014, A&A, 562, A24
McConnachie A. W., Irwin M. J., Ferguson A. M. N., Ibata R. A., Lewis G. F., Tanvir N., 2005, MNRAS, 356, 979
McNally D., 1965, The Obser., 85, 166
McQuinn K. B. W., Skillman E. D., Dalcanton J. J., Dolphin A. E., Holtzman J., Weisz D. R., Williams B. F., 2011, ApJ, 740, 48
Melbourne J. et al., 2012, ApJ, 748, 47
Merrill P. W., 1921, ApJ, 53
Merrill P. W., 1952, JRASC, 46, 181
Miszalski B., Mikołajewska J., Udalski A., 2013, MNRAS, 432, 3186
Newman J. A. et al., 2013, ApJS, 208, 5
Osterbrock D. E., 1989, Astrophysics of gaseous nebulae and active galactic nuclei. University Science Books
Pereira C. B., Schiavon R. P., de Araújo F. X., Landaberry S. J. C., 2001, AJ, 121, 1071
Porter J. M., Rivinius T., 2003, PASP, 115, 1153
Reid W. A., Parker Q. A., 2012, MNRAS, 425, 355
Rosenfield P., Marigo P., Girardi L., Dalcanton J. J., Bressan A., Williams B. F., Dolphin A., 2016, ApJ, 822, 73
Sandin C., Roth M. M., Schönberner D., 2010, PASA, 27, 214
Schild R., Romanishin W., 1976, ApJ, 204, 493
Schwarzschild M., Härm R., 1965, ApJ, 142, 855
Schwarzschild M., Härm R., 1967, ApJ, 150, 961
Sholukhova O. N., Fabrika S. N., Vlasyuk V. V., 1999, Astron. Lett., 25, 14
Stothers R., Chin C.-W., 1968, ApJ, 152, 225
Struve O., 1931, ApJ, 74, 225
Tarasov A. E., Malchenko S. L., 2012, Astron. Lett., 38, 428
Wachter A., Schröder K.-P., Winters J. M., Arndt T. U., Sedlmayr E., 2002, A&A, 384, 452
Warner B., 1972, MNRAS, 159, 95
Whitelock P., Feast M., Catchpole R., 1991, MNRAS, 248, 276
Whitelock P. A., 1986, MNRAS, 219, 525
Whitelock P. A., 2012, Ap&SS, 341, 123
Whitelock P. A., 2013, in IAU Symp., Vol. 289, IAU Symp., de Grijs R., ed., pp. 209–216
Williams B. F. et al., 2014, ApJS, 215, 9
Wisniewski J. P., Bjorkman K. S., 2006, ApJ, 652, 458
Wood P. R., 2000, PASA, 17, 18
Wood P. R., Cahn J. H., 1977, ApJ, 211, 499
Wood P. R., Sebo K. M., 1996, MNRAS, 282, 958
Zurita A., Bresolin F., 2012, MNRAS, 427, 1463

© 2016 RAS, MNRAS **000**, 000–000

APPENDIX A: CATALOGUE OF Hα STARS

Table A1: List of selected Hα stars. The columns contain: object name, Hα star classification, DEIMOS mask name, mask slit number, right ascension (RA), declination (Dec), Hα line EW and error, σ_v and error, Heliocentric velocity (v_{Hel}), R_{deproj}, and the PHAT six-filter photometry. The object names sometimes conflict with the classifications as they are based on an earlier misclassification. Object names in a box relate to the objects that we present a section of their 2D SPLASH spectrum in Appendix B.

Object	Class.	Mask	Slit No.	RA	Dec	Hα EW (Å)	σ_v (km s^{-1})	v_{Hel} (km s^{-1})	R_{deproj} (kpc)	F275W	F336W	F475W	F814W	F110W	F160W
AGB1800	RHeB	mct6B	14	00 : 44 : 12.77	+41 : 06 : 50.4	−3.11 ± 0.10	61 ± 3	−62.8	12.48	-	-	23.65	20.33	19.22	18.32
RGB3554	RHeB?	mct6B	25	00 : 44 : 13.39	+41 : 07 : 27.1	−2.48 ± 0.44	25 ± 14	−343.0	12.27	-	27.62	23.57	21.07	20.26	19.35
AGB4591	RHeB	mct6B	30	00 : 44 : 13.75	+41 : 07 : 43.1	−4.38 ± 0.12	56 ± 4	−112.4	12.19	-	27.82	24.39	20.47	19.41	18.64
AGB17874	AGB	mct6B	61	00 : 44 : 22.05	+41 : 09 : 31.6	−5.25 ± 0.72	58 ± 17	−333.9	12.19	-	28.53	24.13	19.86	18.37	17.19
AGB63507	RHeB	mct6B	104	00 : 44 : 26.16	+41 : 12 : 37.7	−3.78 ± 0.11	59 ± 3	−400.2	11.28	-	-	24.89	20.41	19.13	18.53
AGB65520	AGB	mct6B	106	00 : 44 : 20.56	+41 : 12 : 45.1	−2.37 ± 0.14	46 ± 5	−268.2	10.70	-	27.63	25.28	20.43	18.50	17.57
AGB74155	RHeB	mct6B	117	00 : 44 : 18.71	+41 : 13 : 17.3	−2.68 ± 0.22	76 ± 8	80.6	10.30	-	26.43	22.65	19.78	19.31	18.56
AGB105172	T-MS	mct6B	147	00 : 44 : 25.29	+41 : 15 : 04.7	−0.54 ± 0.04	64 ± 4	−59.1	10.21	-	22.88	21.74	20.35	20.29	19.70
AGB147540	AGB	mct6B	186	00 : 44 : 39.99	+41 : 17 : 34.1	−2.44 ± 0.12	64 ± 5	−295.8	10.67	-	26.83	30.70	20.94	18.14	17.18
AGB154104	RHeB	mct6B	193	00 : 44 : 48.54	+41 : 17 : 55.9	−2.12 ± 0.08	45 ± 3	−578.9	11.36	-	26.65	22.93	19.87	19.25	18.49
AGB158331	RHeB	mct6B	195	00 : 44 : 44.51	+41 : 18 : 09.8	−7.13 ± 0.83	102 ± 21	−480.2	10.88	-	27.99	22.84	20.02	19.35	18.49
AGB167748	AGB	mct6B	201	00 : 44 : 44.89	+41 : 18 : 41.3	−9.48 ± 1.76	65 ± 19	−137.0	10.73	-	27.29	24.24	20.72	19.49	18.60
AGB173678	AGB	mct6B	206	00 : 44 : 32.58	+41 : 19 : 01.0	−11.00 ± 2.69	79 ± 25	−83.8	9.43	-	27.25	25.12	20.62	19.03	18.26
MS178449	MS	mct6B	209	00 : 44 : 29.27	+41 : 19 : 17.4	−13.67 ± 1.09	155 ± 14	−340.9	9.02	22.22	22.13	22.91	21.83	21.01	20.22
AGB187069	RHeB	mct6B	213	00 : 44 : 36.35	+41 : 19 : 46.0	−7.24 ± 2.33	47 ± 21	−272.2	9.53	-	28.28	23.88	19.50	19.02	18.03
MS128721	MS	mct6C	25	00 : 44 : 21.57	+41 : 16 : 26.3	−28.80 ± 2.37	140 ± 16	−255.2	9.33	20.57	20.83	22.38	22.25	22.33	22.15
MS179275	MS	mct6C	64	00 : 44 : 31.66	+41 : 19 : 19.9	−8.53 ± 0.13	102 ± 2	−246.8	9.23	19.17	19.34	20.84	20.65	20.59	20.43
MS185530	MS	mct6C	72	00 : 44 : 37.73	+41 : 19 : 40.7	−8.16 ± 0.13	187 ± 4	−303.4	9.69	19.65	19.74	20.96	20.67	20.96	20.84
MS201708	MS	mct6C	88	00 : 44 : 33.28	+41 : 20 : 34.2	−14.36 ± 0.93	193 ± 10	−92.6	8.96	21.93	21.85	22.80	22.52	22.40	22.29
MS251784	AGB	mct6C	145	00 : 44 : 49.48	+41 : 23 : 00.5	−4.79 ± 0.86	24 ± 27	−208.8	9.69	-	28.63	25.31	21.61	20.28	19.25
MS257904	MS	mct6C	149	00 : 44 : 48.61	+41 : 23 : 14.0	−23.26 ± 1.00	92 ± 11	−278.9	9.54	20.51	20.71	22.11	22.02	21.96	21.82
AGB269781	RHeB	mct6C	158	00 : 44 : 56.46	+41 : 23 : 38.1	−2.75 ± 0.17	64 ± 5	−490.2	10.15	-	26.31	24.06	20.58	19.69	18.97
MS313163	MS	mct6C	180	00 : 45 : 06.98	+41 : 24 : 51.2	−12.60 ± 0.16	141 ± 2	−249.0	10.76	18.97	19.18	20.69	20.52	20.65	20.43
AGB341522	RHeB	mct6C	189	00 : 45 : 18.46	+41 : 25 : 32.3	−4.07 ± 0.18	54 ± 4	−271.3	11.62	-	-	23.13	19.67	19.25	18.53
MS420720	MS	mct6C	211	00 : 45 : 14.27	+41 : 27 : 18.8	−9.39 ± 1.09	113 ± 23	−190.9	10.72	21.77	21.88	22.75	22.71	22.76	22.65
AGB275033	AGB C*	mct6D	35	00 : 44 : 54.60	+41 : 23 : 48.0	−13.90 ± 4.30	62 ± 33	−198.6	9.93	-	-	25.24	19.87	18.75	17.47
AGB289376	RHeB	mct6D	39	00 : 44 : 36.30	+41 : 24 : 13.0	−1.76 ± 0.17	48 ± 8	−252.5	8.11	-	28.15	22.87	19.48	18.33	17.30
MS332202	MS	mct6D	57	00 : 44 : 36.37	+41 : 25 : 19.5	−0.63 ± 0.02	25 ± 3	−271.6	7.82	17.69	17.97	19.37	19.21	19.40	19.32
MS412514	MS	mct6D	80	00 : 44 : 32.07	+41 : 27 : 06.9	−1.95 ± 0.12	52 ± 6	−264.1	7.03	22.04	21.54	22.24	21.20	20.92	20.82
MS118058	MS	mct6E	79	00 : 44 : 04.57	+41 : 15 : 47.6	−14.25 ± 1.26	195 ± 22	−193.6	7.94	21.19	21.07	22.36	21.78	21.74	21.47
SG127353	T-MS	mct6E	84	00 : 44 : 04.80	+41 : 16 : 21.2	−8.93 ± 0.63	225 ± 15	−310.6	7.75	23.32	21.96	21.39	20.88	20.78	20.31
MS181868	AGB	mct6E	123	00 : 44 : 02.67	+41 : 19 : 28.4	−17.40 ± 1.49	206 ± 24	−414.0	6.42	-	-	26.25	21.83	20.29	19.27
MS223912	T-MS	mct6E	161	00 : 43 : 52.05	+41 : 21 : 47.4	−9.25 ± 0.93	83 ± 13	−104.6	4.74	22.04	21.32	21.54	21.20	21.15	21.00
MS310616	MS	mct6E	204	00 : 43 : 57.06	+41 : 24 : 47.3	−15.64 ± 2.37	115 ± 31	−221.8	4.56	21.82	21.25	21.81	21.06	20.99	20.81
MS341793	MS	mct6E	214	00 : 43 : 56.05	+41 : 25 : 32.7	−25.33 ± 1.49	135 ± 18	−114.6	4.38	19.55	19.86	21.50	21.39	21.62	21.24
AGB362536	AGB C*	mct6E	218	00 : 43 : 58.57	+41 : 26 : 00.6	−3.49 ± 0.51	65 ± 14	−252.9	4.52	-	-	26.10	19.83	17.68	16.66
AGB543679	RHeB	mct6F	14	00 : 45 : 53.07	+41 : 34 : 35.4	−4.47 ± 0.19	69 ± 5	−259.0	12.37	-	25.97	22.98	20.02	19.49	18.62
AGB568802	RHeB	mct6F	34	00 : 45 : 56.13	+41 : 36 : 10.2	−5.35 ± 0.17	55 ± 3	−173.6	12.31	-	-	22.45	19.61	19.28	18.57
AGB646278	AGB	mct6F	70	00 : 45 : 59.91	+41 : 39 : 06.3	−7.93 ± 1.50	72 ± 18	−36.5	12.10	-	-	24.83	20.02	18.63	17.62
AGB686015	RHeB	mct6F	93	00 : 45 : 57.69	+41 : 41 : 09.9	−1.94 ± 0.07	48 ± 4	−333.2	11.66	-	-	22.40	19.56	19.46	18.79
AGB692878	AGB	mct6F	98	00 : 45 : 47.09	+41 : 41 : 37.0	−0.55 ± 0.10	11 ± 7	−202.9	10.87	-	26.36	24.08	20.56	19.31	18.22
MS692952	MS	mct6F	99	00 : 45 : 54.30	+41 : 41 : 37.3	−20.90 ± 1.75	138 ± 16	−220.6	11.37	22.51	22.32	22.96	22.83	22.80	22.76
MS700544	MS	mct6F	108	00 : 45 : 53.87	+41 : 42 : 09.7	−22.96 ± 0.33	121 ± 4	−184.2	11.29	19.81	19.95	21.21	21.05	21.11	20.94
AGB708605	AGB	mct6F	118	00 : 45 : 51.83	+41 : 42 : 49.9	−4.20 ± 1.02	40 ± 28	−67.0	11.11	-	27.26	25.84	20.38	18.22	17.17
AGB709905	AGB	mct6F	121	00 : 46 : 00.65	+41 : 42 : 56.7	−3.22 ± 0.23	69 ± 7	−304.0	11.70	-	27.13	24.40	20.77	19.60	18.64
MS761954	MS	mct6F	194	00 : 46 : 08.86	+41 : 47 : 58.5	−15.85 ± 0.61	112 ± 9	−186.3	12.01	20.46	20.55	21.88	21.46	21.51	21.28
MS763520	MS	mct6F	200	00 : 46 : 11.14	+41 : 48 : 07.6	−25.73 ± 1.40	170 ± 11	−174.8	12.15	21.71	21.60	22.86	22.30	22.23	21.87
MS775105	MS	mct6F	210	00 : 46 : 07.52	+41 : 49 : 14.2	−7.81 ± 0.16	212 ± 4	−66.4	11.95	19.40	19.72	21.25	21.14	21.24	21.06
MS575747	MS	mct6G	11	00 : 45 : 16.67	+41 : 36 : 28.9	−28.81 ± 1.22	169 ± 8	−153.2	9.16	19.87	19.94	21.34	20.78	20.65	20.34
MS661443	AGB	mct6G	59	00 : 45 : 36.47	+41 : 39 : 45.1	−21.63 ± 0.54	118 ± 5	−153.6	10.27	-	-	25.99	20.45	18.81	17.78
MS683060	MS	mct6G	74	00 : 45 : 27.79	+41 : 40 : 58.2	−3.53 ± 0.12	99 ± 4	−80.7	9.64	20.12	20.25	21.29	21.19	21.19	21.12

Object	Class.	Mask	Slit No.	RA	Dec	Hα EW (Å)			σ_v (km s^{-1})			v_{Hel} (km s^{-1})	R_{deproj} (kpc)	F275W	F336W	F475W	F814W	F110W	F160W
MS708596	AGB	mct6G	105	00 : 45 : 32.67	+41 : 42 : 49.8	−6.26	±	0.28	166	±	8	−140.4	9.91	-	30.65	25.43	21.02	19.23	18.19
MS716320	MS	mct6G	113	00 : 45 : 44.32	+41 : 43 : 32.5	−1.92	±	0.02	72	±	1	−156.2	10.6	17.10	17.18	18.50	18.11	18.14	18.02
MS722500	MS	mct6G	124	00 : 45 : 41.94	+41 : 44 : 08.4	−36.40	±	0.63	109	±	4	−170.8	10.45	19.26	19.31	20.75	20.32	20.36	20.06
MS723461	MS	mct6G	126	00 : 45 : 39.20	+41 : 44 : 14.1	−23.02	±	0.67	87	±	4	−85.4	10.29	20.51	20.33	21.26	20.85	20.92	20.77
MS729737	MS	mct6G	138	00 : 45 : 47.66	+41 : 44 : 52.1	−26.98	±	0.99	158	±	11	−199.0	10.78	20.63	20.66	21.92	21.46	21.43	21.18
MS742327	MS	mct6G	161	00 : 45 : 56.06	+41 : 46 : 07.0	−33.49	±	3.58	108	±	14	−228.4	11.27	21.63	21.54	22.34	21.87	21.76	21.44
MS763598	MS	mct6G	193	00 : 46 : 08.20	+41 : 48 : 08.0	−5.83	±	0.27	268	±	7	−191.4	11.97	20.51	20.55	21.63	21.56	21.59	21.56
MS767158	MS	mct6G	198	00 : 46 : 07.10	+41 : 48 : 28.6	−4.05	±	0.08	162	±	3	−212.4	11.91	18.79	18.99	20.36	20.18	20.26	20.23
MS767515	MS	mct6G	199	00 : 45 : 56.11	+41 : 48 : 30.7	−11.75	±	0.36	143	±	7	−231.6	11.32	20.36	20.45	21.82	21.33	21.31	21.08
MS779790	MS	mct6G	211	00 : 45 : 48.81	+41 : 49 : 35.8	−28.62	±	0.30	104	±	5	−83.9	11.06	17.96	18.22	19.94	19.50	19.54	19.27
MS597687	MS	mct6H	21	00 : 45 : 06.06	+41 : 37 : 18.9	−10.37	±	0.18	110	±	4	−196.2	8.38	18.01	18.30	19.84	19.78	19.97	19.81
MS608785	MS	mct6H	29	00 : 45 : 14.69	+41 : 37 : 43.3	−2.89	±	0.03	90	±	1	−185.3	8.92	17.65	17.88	19.32	19.20	19.38	19.33
MS634466	MS	mct6H	42	00 : 45 : 15.29	+41 : 38 : 39.0	−47.31	±	1.95	113	±	11	−139.4	8.92	19.88	20.02	21.62	21.40	21.42	21.17
AGB637838	RHeB	mct6H	46	00 : 45 : 08.79	+41 : 38 : 46.7	−2.71	±	0.17	41	±	6	−368.2	8.52	-	25.60	22.37	19.39	18.60	17.92
MS698062	MS	mct6H	92	00 : 45 : 19.91	+41 : 41 : 58.5	−2.22	±	0.10	103	±	5	−164.4	9.19	20.86	20.66	21.59	20.91	20.67	20.49
MS703326	MS	mct6H	101	00 : 45 : 26.09	+41 : 42 : 22.7	−6.77	±	0.43	174	±	12	−127.2	9.54	21.10	21.11	21.95	21.75	21.87	21.77
MS710772	MS	mct6H	107	00 : 45 : 22.30	+41 : 43 : 01.6	−49.61	±	10.16	162	±	31	−223.8	9.36	21.08	21.24	22.49	22.32	22.63	22.66
AGB727603	MS	mct6H	131	00 : 45 : 28.91	+41 : 44 : 39.2	−2.24	±	0.13	45	±	5	−158.8	9.77	21.99	21.49	22.11	20.85	20.68	20.44
MS755421	MS	mct6H	170	00 : 45 : 29.94	+41 : 47 : 20.9	−6.19	±	0.29	382	±	9	−148.9	10.07	20.89	20.82	21.94	21.34	21.15	20.88
AGB799233	RHeB	mct6H	216	00 : 45 : 41.72	+41 : 50 : 45.6	−2.53	±	0.17	81	±	7	−92.7	10.94	-	25.69	23.15	20.48	19.55	18.67
MS249482	MS	mct6I	17	00 : 43 : 39.02	+41 : 22 : 55.1	−22.27	±	0.52	154	±	6	−218.0	3.41	19.09	19.27	20.86	20.53	20.35	20.08
MS257350	MS	mct6I	27	00 : 43 : 33.43	+41 : 23 : 12.9	−23.29	±	0.53	153	±	8	−138.2	2.97	19.36	19.62	21.09	20.80	20.83	20.50
MS267013	MS	mct6I	45	00 : 43 : 43.99	+41 : 23 : 32.8	−13.47	±	0.42	140	±	6	−177.5	3.71	19.85	19.98	21.17	20.78	20.74	20.33
MS272171	T-MS	mct6I	51	00 : 43 : 57.55	+41 : 23 : 42.8	−12.81	±	0.47	52	±	8	−332.4	4.79	21.62	20.65	21.09	20.51	20.34	20.21
serendip1	AGB	mct6I	54	00 : 44 : 17.25	+41 : 23 : 45.8	−0.78	±	0.07	45	±	4	−246.7	6.50	-	-	25.40	20.17	18.27	17.13
MS275061	T-MS	mct6I	57	00 : 43 : 27.94	+41 : 23 : 48.0	−7.91	±	0.25	50	±	5	−252.8	2.64	21.34	20.47	20.74	20.25	20.31	20.08
MS277924	T-MS	mct6I	63	00 : 43 : 56.91	+41 : 23 : 53.2	−6.73	±	0.24	124	±	6	−231.0	4.70	22.11	21.58	21.67	20.95	20.52	19.97
MS283118	MS	mct6I	71	00 : 43 : 36.25	+41 : 24 : 02.5	−20.78	±	0.83	118	±	7	−127.6	3.12	19.49	19.73	21.22	21.03	21.28	21.10
serendip1	MS	mct6I	71	00 : 43 : 36.38	+41 : 24 : 02.6	−6.00	±	0.75	46	±	14	−104.5	3.13	22.69	22.07	22.73	21.92	21.73	21.67
MS285212	T-MS	mct6I	73	00 : 43 : 42.35	+41 : 24 : 06.1	−1.18	±	0.05	74	±	4	−114.8	3.53	22.49	21.35	20.97	20.44	20.48	20.19
MS285376	MS	mct6I	76	00 : 44 : 34.37	+41 : 24 : 06.4	−3.54	±	0.11	199	±	6	−264.8	7.97	18.89	19.15	20.62	20.69	20.99	21.03
AGB287947	T-MS	mct6I	80	00 : 44 : 31.62	+41 : 24 : 10.7	−9.62	±	0.18	121	±	6	−254.8	7.69	22.02	21.27	20.64	19.15	18.67	18.21
AGB295890	RHeB	mct6I	91	00 : 44 : 25.36	+41 : 24 : 24.0	−4.91	±	0.17	75	±	4	−288.8	7.07	-	25.85	23.65	19.94	19.11	18.25
MS310626	MS	mct6I	118	00 : 43 : 53.31	+41 : 24 : 47.3	−1.33	±	0.01	134	±	1	−189.4	4.27	16.81	17.21	18.84	18.89	18.89	18.37
AGB325404	AGB C*	mct6I	134	00 : 44 : 22.14	+41 : 25 : 09.8	−4.64	±	0.35	187	±	9	−236.6	6.60	-	-	24.03	19.65	18.03	16.94
MS338932	MS	mct6I	146	00 : 44 : 34.43	+41 : 25 : 28.7	−50.33	±	0.55	87	±	7	−223.4	7.61	18.72	18.65	19.75	19.28	19.25	19.01
AGB344610	AGB C*	mct6I	151	00 : 44 : 15.78	+41 : 25 : 36.7	−2.37	±	0.21	59	±	6	−225.2	5.95	-	-	24.62	19.76	18.18	16.95
MS355973	MS	mct6I	159	00 : 43 : 40.77	+41 : 25 : 51.9	−16.83	±	1.23	52	±	11	−390.5	3.40	20.78	20.52	21.64	21.20	21.07	20.87
serendip1	AGB	mct6I	168	00 : 44 : 39.22	+41 : 25 : 59.2	−10.95	±	1.83	88	±	43	−216.0	7.91	-	-	26.58	21.76	20.01	18.81
MS373085	T-MS	mct6I	179	00 : 44 : 13.36	+41 : 26 : 14.3	−1.85	±	0.12	38	±	5	−93.7	5.63	-	21.06	21.02	20.75	20.66	20.57
MS380470	MS	mct6I	188	00 : 44 : 20.53	+41 : 26 : 23.9	−9.01	±	0.22	210	±	6	−302.2	6.20	19.89	19.99	21.38	20.96	21.05	20.78
MS392298	MS	mct6I	197	00 : 44 : 52.59	+41 : 26 : 39.3	−4.08	±	0.20	89	±	8	−339.8	8.93	21.31	21.35	22.38	22.05	21.98	21.89
MS578990	MS	mct6K	60	00 : 44 : 32.21	+41 : 36 : 37.0	−14.86	±	0.27	128	±	4	−75.6	6.60	18.48	18.78	20.39	20.17	20.25	20.04
MS579231	MS	mct6K	61	00 : 43 : 58.04	+41 : 36 : 37.6	−23.38	±	2.59	119	±	11	−166.7	6.11	20.73	20.85	21.89	21.78	21.96	21.75
MS587961	MS	mct6K	75	00 : 44 : 27.40	+41 : 36 : 57.6	−17.85	±	0.86	211	±	10	−175.6	6.49	20.26	20.41	21.45	21.38	21.55	21.56
MS594977	T-MS	mct6K	84	00 : 45 : 06.13	+41 : 37 : 13.0	−4.53	±	1.22	93	±	16	−73.4	8.39	23.60	22.96	22.56	22.06	22.14	21.89
serendip1	MS	mct6K	93	00 : 45 : 04.96	+41 : 37 : 26.9	−1.14	±	0.02	78	±	2	−112.1	8.31	16.70	16.93	18.43	18.34	18.49	18.46
MS602034	MS	mct6K	97	00 : 45 : 19.73	+41 : 37 : 28.4	−9.32	±	0.37	179	±	9	−183.2	9.29	21.31	21.19	21.98	21.42	21.41	21.17
serendip1	RHeB	mct6K	98	00 : 44 : 53.13	+41 : 37 : 28.8	−2.88	±	0.52	53	±	12	−173.5	7.63	-	32.97	25.04	20.88	-	-
MS607506	T-MS	mct6K	113	00 : 45 : 20.77	+41 : 37 : 40.5	−5.07	±	1.08	65	±	16	−155.5	9.34	22.26	21.80	21.53	21.19	21.09	21.03
MS613247	MS	mct6K	123	00 : 44 : 43.41	+41 : 37 : 53.0	−40.88	±	1.62	155	±	8	−136.5	7.19	20.66	20.69	21.95	21.48	21.51	21.33
MS623672	AGB	mct6K	155	00 : 45 : 12.73	+41 : 38 : 15.2	−3.29	±	0.55	55	±	14	−152.8	8.77	-	-	25.79	21.46	19.60	18.62
MS642835	MS	mct6K	181	00 : 45 : 17.06	+41 : 38 : 58.2	−1.71	±	0.03	96	±	3	−92.1	9.02	17.05	16.56	17.76	16.80	16.69	16.62
MS918576	MS	mct6L	53	00 : 45 : 59.77	+41 : 57 : 14.9	−6.48	±	1.23	58	±	11	−124.0	12.55	21.60	21.70	22.61	22.65	22.82	22.81
MS966060	MS	mct6L	104	00 : 46 : 10.38	+42 : 01 : 02.9	−6.72	±	0.60	92	±	15	−94.1	13.56	23.06	22.65	22.93	22.68	22.68	22.60
AGB1008239	AGB	mct6L	210	00 : 45 : 39.04	+42 : 07 : 30.9	−1.80	±	0.37	48	±	8	−150.2	15.53	-	-	25.29	20.30	18.55	17.45
MS1018382	AGB	mct6L	227	00 : 45 : 52.62	+42 : 08 : 46.4	−11.97	±	0.73	158	±	7	−186.1	15.76	-	27.28	25.41	22.35	21.27	20.29
MS388051	MS	mct6M	35	00 : 44 : 45.17	+41 : 26 : 33.8	−8.49	±	0.33	195	±	8	−231.3	8.29	20.44	20.38	21.31	20.78	20.65	20.48
SG406459	T-MS	mct6M	47	00 : 44 : 46.06	+41 : 26 : 58.4	−3.82	±	0.38	71	±	10	−190.7	8.27	-	23.12	22.25	21.22	20.88	20.68
MS434008	MS	mct6M	55	00 : 44 : 41.15	+41 : 27 : 38.8	−9.75	±	0.73	149	±	14	−247.7	7.69	21.06	21.07	21.92	21.73	21.91	21.85
MS440713	MS	mct6M	57	00 : 44 : 33.60	+41 : 27 : 49.1	−11.33	±	0.58	166	±	10	−297.3	7.02	22.39	21.81	22.41	21.19	20.93	20.62
MS454607	MS	mct6M	61	00 : 44 : 47.22	+41 : 28 : 11.7	−2.67	±	0.09	56	±	4	−192.3	8.10	19.40	19.43	20.49	20.17	20.21	20.17
MS507660	MS	mct6M	83	00 : 44 : 49.18	+41 : 30 : 03.5	−6.12	±	0.49	62	±	8	−215.9	7.90	19.97	20.26	21.67	21.61	21.67	21.43

Object	Class.	Mask	Slit No.	RA	Dec	Hα EW (Å)	σ_v (km s^{-1})	v$_{Hel}$ (km s^{-1})	R$_{deproj}$ (kpc)	F275W	F336W	F475W	F814W	F110W	F160W
MS514797	MS	mct6M	90	00 : 44 : 46.83	+41 : 30 : 27.9	−3.08 ± 0.27	47 ± 8	−191.2	7.64	19.32	19.47	20.72	20.48	20.58	20.53
MS527247	MS	mct6M	105	00 : 44 : 37.98	+41 : 31 : 36.2	−5.10 ± 0.45	67 ± 9	−229.1	6.83	20.97	20.90	21.99	21.75	21.72	21.68
MS540379	MS	mct6M	137	00 : 44 : 41.60	+41 : 34 : 17.3	−6.20 ± 0.42	93 ± 7	−211.6	6.94	20.24	20.25	21.47	21.00	20.92	20.66
MS548831	MS	mct6M	142	00 : 44 : 23.37	+41 : 35 : 00.1	−14.35 ± 0.69	99 ± 7	−189.7	6.07	20.37	20.39	21.45	21.09	21.47	21.18
AGB571711	T-MS	mct6M	156	00 : 44 : 30.54	+41 : 36 : 18.4	−6.05 ± 0.88	50 ± 11	−135.9	6.50	-	23.55	22.47	21.07	20.62	20.15
MS579806	MS	mct6M	160	00 : 44 : 36.52	+41 : 36 : 39.0	−8.74 ± 0.38	82 ± 7	−244.3	6.78	19.63	19.92	21.09	21.04	21.23	21.18
MS582186	MS	mct6M	161	00 : 44 : 19.15	+41 : 36 : 44.7	−48.07 ± 11.23	83 ± 30	−182.6	6.25	21.37	21.45	22.47	22.35	22.41	22.23
RGB635965	RHeB?	mct6M	185	00 : 44 : 20.76	+41 : 38 : 42.4	−3.90 ± 0.36	50 ± 11	−63.1	6.73	-	24.78	23.07	20.84	20.13	19.54
MS673940	MS	mct6M	208	00 : 44 : 23.36	+41 : 40 : 24.9	−10.28 ± 0.26	120 ± 5	−137.0	7.21	20.38	20.40	21.53	21.32	21.48	21.33
SG770695	T-MS	mct6O	13	00 : 45 : 36.17	+41 : 48 : 49.2	−2.77 ± 0.03	114 ± 2	−94.5	10.48	21.33	19.48	18.40	16.71	16.26	15.88
MS790086	MS	mct6O	40	00 : 45 : 38.25	+41 : 50 : 15.7	−23.21 ± 5.12	51 ± 51	−71.0	10.75	22.48	22.08	22.97	22.22	22.07	21.89
serendip1	RHeB	mct6O	76	00 : 45 : 25.91	+41 : 51 : 16.1	−27.81 ± 1.91	152 ± 17	−142.7	10.62	-	-	24.94	22.73	22.06	21.27
MS829713	MS	mct6O	123	00 : 44 : 52.83	+41 : 52 : 17.3	−0.55 ± 0.01	63 ± 1	−58.8	10.82	18.17	18.19	19.41	18.90	18.87	18.77
MS829767	MS	mct6O	124	00 : 44 : 32.23	+41 : 52 : 17.5	−7.63 ± 0.86	60 ± 15	−186.3	11.26	21.96	21.57	22.10	21.31	21.03	20.81
MS833627	MS	mct6O	138	00 : 45 : 38.26	+41 : 52 : 28.5	−23.1 ± 1.35	64 ± 10	−105.7	11.13	19.36	19.60	21.03	20.94	21.08	21.09
MS838996	MS	mct6O	154	00 : 44 : 52.25	+41 : 52 : 43.4	−21.19 ± 0.98	194 ± 11	−193.6	10.98	19.97	20.06	21.46	20.97	20.97	20.70
MS843459	MS	mct6O	162	00 : 45 : 13.19	+41 : 52 : 56.6	−11.51 ± 0.92	198 ± 17	−76.4	10.92	20.42	20.53	21.82	21.67	21.98	21.89
MS854403	MS	mct6O	186	00 : 45 : 19.69	+41 : 53 : 28.7	−19.66 ± 1.31	114 ± 26	−212.3	11.09	19.99	20.22	21.68	21.51	21.67	21.46
MS864633	MS	mct6O	207	00 : 45 : 04.81	+41 : 53 : 59.3	−43.46 ± 1.67	97 ± 9	−98.9	11.27	19.93	19.88	21.09	20.49	20.43	20.14
serendip1	AGB	mct6O	208	00 : 44 : 36.21	+41 : 54 : 00.2	−33.94 ± 7.84	77 ± 79	−173.9	11.83	-	-	26.40	21.22	19.28	18.17
serendip1	AGB	mct6O	236	00 : 44 : 49.90	+41 : 52 : 42.0	−14.99 ± 0.68	62 ± 6	−52.3	11.01	-	27.27	27.43	22.51	18.49	18.03
AGB844835	AGB	mct6P	32	00 : 46 : 10.16	+41 : 53 : 00.7	−9.84 ± 2.29	52 ± 43	−82.8	12.29	-	28.99	26.00	20.58	18.39	17.35
MS854153	MS	mct6P	46	00 : 45 : 35.18	+41 : 53 : 27.9	−6.04 ± 0.52	51 ± 35	−78.0	11.27	21.36	21.42	22.34	22.21	22.26	22.20
MS862789	T-MS	mct6P	66	00 : 45 : 41.73	+41 : 53 : 53.7	−12.75 ± 0.22	123 ± 7	−94.7	11.49	19.85	19.22	19.19	18.84	18.76	18.48
MS883034	MS	mct6P	115	00 : 45 : 31.87	+41 : 55 : 02.4	−11.11 ± 0.48	99 ± 6	−148.7	11.60	17.99	18.50	20.19	20.45	20.73	20.81
MS890980	MS	mct6P	137	00 : 44 : 53.13	+41 : 55 : 32.4	−0.71 ± 0.17	15 ± 7	−113.0	12.00	20.13	20.03	20.98	20.40	20.32	20.23
MS892450	MS	mct6P	142	00 : 46 : 05.18	+41 : 55 : 37.7	−15.50 ± 1.44	168 ± 11	−152.8	12.41	20.16	20.25	21.60	21.46	21.50	21.39
MS897001	MS	mct6P	155	00 : 44 : 56.71	+41 : 55 : 54.8	−17.38 ± 2.34	113 ± 37	−88.2	12.06	22.25	22.17	22.85	22.70	22.70	22.64
MS898676	MS	mct6P	159	00 : 45 : 42.08	+41 : 56 : 01.1	−2.14 ± 0.01	297 ± 2	−79.3	11.96	16.11	-	17.26	16.97	17.03	16.94
MS921236	MS	mct6P	197	00 : 45 : 10.16	+41 : 57 : 25.8	−28.27 ± 1.36	171 ± 8	−156.8	12.38	19.98	20.19	21.75	21.46	21.44	21.21
MS925371	MS	mct6P	199	00 : 45 : 02.67	+41 : 57 : 41.9	−29.68 ± 1.78	100 ± 6	−111.0	12.61	19.62	19.84	21.11	20.91	21.20	21.01
MS924898	MS	mct6Q	31	00 : 45 : 11.82	+41 : 57 : 40.0	−26.03 ± 2.36	147 ± 20	−110.7	12.44	20.66	20.88	22.26	22.17	22.31	22.17
AGB928293	AGB C*	mct6Q	36	00 : 46 : 16.55	+41 : 57 : 54.0	−6.48 ± 0.47	62 ± 6	−132.3	13.12	-	-	25.30	19.80	17.76	16.65
MS933068	MS	mct6Q	48	00 : 45 : 54.98	+41 : 58 : 14.4	−5.18 ± 0.25	175 ± 9	−190.7	12.67	21.24	21.15	21.88	21.43	21.48	21.33
MS936504	MS	mct6Q	62	00 : 45 : 28.26	+41 : 58 : 29.2	−12.55 ± 1.25	144 ± 17	−167.0	12.57	22.14	21.94	22.86	22.20	21.75	21.68
MS938750	MS	mct6Q	72	00 : 45 : 36.02	+41 : 58 : 39.2	−12.12 ± 0.31	174 ± 7	−185.8	12.61	19.95	20.13	21.48	21.28	21.37	21.20
MS942221	MS	mct6Q	83	00 : 45 : 43.63	+41 : 58 : 54.7	−14.37 ± 0.32	220 ± 4	−141.6	12.71	20.17	20.08	21.28	20.60	20.54	20.29
MS942322	MS	mct6Q	84	00 : 45 : 28.28	+41 : 58 : 55.2	−25.95 ± 0.78	158 ± 6	−100.3	12.71	20.69	20.51	21.59	20.93	20.88	20.52
MS944360	MS	mct6Q	95	00 : 45 : 44.20	+41 : 59 : 04.8	−17.33 ± 0.62	141 ± 8	−106.8	12.76	20.17	20.19	21.39	21.02	21.07	20.88
MS944642	MS	mct6Q	96	00 : 45 : 03.54	+41 : 59 : 06.1	−7.24 ± 0.24	111 ± 4	−70.2	13.11	18.84	19.09	20.55	20.48	20.56	20.52
serendip1	AGB	mct6Q	96	00 : 45 : 03.44	+41 : 59 : 06.3	−13.05 ± 2.81	68 ± 37	−95.4	13.12	-	-	26.24	20.82	18.53	17.36
MS950027	MS	mct6Q	116	00 : 45 : 01.60	+41 : 59 : 30.4	−3.70 ± 0.27	47 ± 7	−118.7	13.31	21.08	20.76	21.74	20.77	20.51	20.32
MS960668	MS	mct6Q	148	00 : 45 : 18.17	+42 : 00 : 26.5	−25.09 ± 1.32	100 ± 7	−153.8	13.33	20.88	20.98	21.81	21.73	21.93	21.81
MS963896	MS	mct6Q	155	00 : 44 : 56.74	+42 : 00 : 47.7	−21.35 ± 5.58	102 ± 43	−129.6	13.95	21.76	21.71	22.48	22.30	22.36	22.24
MS967879	MS	mct6Q	172	00 : 44 : 59.89	+42 : 01 : 16.1	−21.77 ± 1.98	123 ± 14	−181.8	14.05	21.13	21.15	22.59	22.53	22.30	22.14
MS1023626	MS	mct6R	21	00 : 47 : 23.76	+42 : 09 : 28.4	−13.82 ± 0.80	91 ± 10	−198.1	16.99	21.75	21.68	22.47	22.33	22.42	22.37
AGB1025281	AGB	mct6R	27	00 : 47 : 13.76	+42 : 09 : 42.4	−1.47 ± 0.26	51 ± 9	−340.2	16.71	-	26.10	27.53	21.72	18.50	17.57
MS1026522	MS	mct6R	32	00 : 47 : 17.84	+42 : 09 : 53.1	−15.45 ± 1.72	82 ± 19	−95.2	16.86	22.41	22.06	22.64	22.32	22.25	22.22
MS1027514	MS	mct6R	41	00 : 47 : 34.26	+42 : 10 : 01.5	−38.32 ± 0.75	101 ± 5	−141.6	17.44	19.58	19.80	21.22	21.05	21.35	21.06
MS1032330	MS	mct6R	70	00 : 46 : 39.30	+42 : 10 : 43.4	−6.83 ± 0.58	63 ± 13	−94.0	16.26	20.44	20.50	22.14	21.67	21.19	21.00
MS1035086	MS	mct6R	91	00 : 46 : 47.68	+42 : 11 : 06.4	−3.84 ± 0.2	63 ± 9	−201.8	16.45	21.36	21.35	21.92	21.73	21.79	21.71
MS1036341	MS	mct6R	100	00 : 46 : 49.93	+42 : 11 : 16.4	−30.42 ± 0.35	128 ± 3	−134.0	16.52	18.97	19.22	20.82	20.56	20.62	20.40
MS1037476	MS	mct6R	109	00 : 46 : 59.50	+42 : 11 : 25.2	−18.66 ± 0.22	165 ± 2	−161.3	16.70	19.39	19.51	20.81	20.65	20.69	20.51
MS1037726	MS	mct6R	111	00 : 47 : 29.15	+42 : 11 : 27.4	−27.72 ± 0.54	152 ± 3	−111.8	17.45	19.72	19.76	21.09	20.71	20.79	20.50
MS1037909	T-MS	mct6R	115	00 : 47 : 10.11	+42 : 11 : 28.8	−3.81 ± 0.11	105 ± 5	−146.2	16.93	20.97	20.77	21.01	20.81	20.79	20.71
MS1039213	MS	mct6R	128	00 : 46 : 20.78	+42 : 11 : 39.4	−29.94 ± 1.92	115 ± 14	−121.3	16.48	22.08	21.81	22.81	22.03	21.89	21.60
MS1040439	MS	mct6R	139	00 : 46 : 44.66	+42 : 11 : 49.2	−29.16 ± 1.86	135 ± 14	−77.6	16.59	21.32	21.38	22.69	22.24	22.16	21.89
MS1042778	MS	mct6R	157	00 : 47 : 13.78	+42 : 12 : 10.4	−10.06 ± 0.41	120 ± 12	−82.0	17.15	20.32	20.44	21.81	21.57	21.69	21.43
MS1043257	MS	mct6R	162	00 : 46 : 20.07	+42 : 12 : 15.4	−5.40 ± 0.20	273 ± 7	−188.6	16.67	19.81	20.07	21.20	21.27	21.37	21.39
MS1045217	MS	mct6R	177	00 : 46 : 36.83	+42 : 12 : 34.9	−23.91 ± 0.74	112 ± 8	−87.2	16.75	21.27	21.11	22.02	21.32	21.21	20.94
MS1045832	MS	mct6R	184	00 : 46 : 58.01	+42 : 12 : 40.9	−2.25 ± 0.58	67 ± 16	−37.4	16.96	21.08	21.35	22.63	22.60	22.64	22.61
MS1048995	MS	mct6R	197	00 : 46 : 36.74	+42 : 13 : 16.4	−16.60 ± 1.54	104 ± 21	−62.4	16.95	22.64	22.49	22.79	22.39	22.23	22.14
MS1008068	MS	mct6S	43	00 : 47 : 05.00	+42 : 07 : 29.7	−60.13 ± 15.08	91 ± 41	−55.5	16.09	21.76	21.64	22.88	22.57	22.61	22.42

© 2016 RAS, MNRAS **000**, 000–000

Object	Class.	Mask	Slit No.	RA	Dec	Hα EW (Å)			σ_v (km s^{-1})			v$_{Hel}$ (km s^{-1})	R$_{deproj}$ (kpc)	F275W	F336W	F475W	F814W	F110W	F160W
MS1009654	MS	mct6S	53	00 : 46 : 47.40	+42 : 07 : 41.4	−35.02	±	1.78	110	±	27	−76.6	15.68	20.38	20.33	21.74	21.13	20.65	20.23
AGB1011804	AGB C*	mct6S	62	00 : 47 : 36.12	+42 : 07 : 57.5	−7.76	±	0.44	63	±	5	−189.8	17.31	-	-	23.53	19.39	17.92	16.88
MS1016968	MS	mct6S	90	00 : 46 : 26.88	+42 : 08 : 36.0	−21.65	±	0.92	251	±	15	−59.9	15.60	19.16	19.37	20.88	20.53	20.55	20.31
MS1024667	MS	mct6S	145	00 : 46 : 29.69	+42 : 09 : 37.2	−17.66	±	0.63	110	±	7	−67.3	15.90	19.80	19.88	20.98	20.72	20.79	20.60
MS1029029	MS	mct6S	174	00 : 46 : 36.91	+42 : 10 : 14.6	−54.09	±	2.71	94	±	11	−110.4	16.12	20.30	20.32	21.54	21.07	21.23	20.95
AGB925447	RHeB	mct6T	71	00 : 45 : 59.19	+41 : 57 : 42.2	−3.67	±	0.17	49	±	5	−73.7	12.63	-	27.24	24.28	20.13	18.99	18.18
MS934267	MS	mct6T	83	00 : 45 : 54.98	+41 : 58 : 19.4	−14.80	±	1.01	65	±	7	−116.0	12.69	21.29	21.34	22.09	21.94	21.96	21.92
MS947307	MS	mct6T	97	00 : 46 : 05.58	+41 : 59 : 18.1	−22.08	±	0.52	91	±	7	−118.0	13.09	19.22	19.53	21.06	20.93	21.10	20.90
AGB952727	AGB	mct6T	105	00 : 45 : 49.67	+41 : 59 : 43.6	−2.01	±	0.10	77	±	5	−134.6	12.97	-	28.84	24.42	20.25	18.93	17.88
MS959219	MS	mct6T	113	00 : 45 : 48.10	+42 : 00 : 17.7	−11.76	±	0.29	226	±	5	−66.3	13.12	19.91	20.16	21.61	21.45	21.65	21.54
AGB989533	AGB C*	mct6T	202	00 : 45 : 24.03	+42 : 04 : 31.2	−0.35	±	0.09	57	±	5	−126.3	14.71	-	27.48	24.31	19.94	18.47	17.28
AGB1001394	RHeB	mct6T	230	00 : 45 : 34.31	+42 : 06 : 37.9	−6.92	±	0.13	77	±	3	−633.6	15.29	-	29.71	22.19	19.40	19.16	18.52
MS1002698	MS	mct6T	234	00 : 45 : 25.11	+42 : 06 : 48.6	−52.43	±	6.04	124	±	29	−194.6	15.56	20.93	21.10	22.33	22.17	22.28	22.10
AGB1005555	AGB	mct6T	240	00 : 45 : 34.70	+42 : 07 : 11.2	−6.17	±	0.49	68	±	8	−311.4	15.49	-	26.36	24.65	20.66	19.25	18.20
MS1031822	MS	mct6U	41	00 : 45 : 48.03	+42 : 10 : 38.5	−5.62	±	0.73	57	±	13	−103.7	16.51	20.02	20.21	21.61	21.60	21.66	-
MS1041161	MS	mct6U	60	00 : 45 : 52.07	+42 : 11 : 55.4	−39.32	±	1.19	130	±	9	−134.2	16.90	21.23	20.88	21.84	20.81	20.55	20.19
MS1042767	MS	mct6U	64	00 : 46 : 06.20	+42 : 12 : 10.3	−23.87	±	6.48	51	±	28	−82.2	16.77	21.34	21.43	22.60	22.45	22.51	22.56
MS1050499	MS	mct6U	98	00 : 45 : 45.04	+42 : 13 : 33.8	−21.17	±	1.91	106	±	12	−142.8	17.68	20.87	21.04	22.11	21.99	22.06	21.99
AGB1052705	AGB C*	mct6U	113	00 : 45 : 55.27	+42 : 13 : 59.7	−3.58	±	0.33	53	±	9	−228.5	17.61	-	-	24.55	20.07	18.73	17.67
MS1059485	MS	mct6U	153	00 : 46 : 19.31	+42 : 15 : 36.9	−3.34	±	0.21	88	±	6	−123.0	17.79	18.89	19.21	20.60	20.71	20.87	20.91
AGB1060489	AGB C*	mct6U	160	00 : 46 : 32.55	+42 : 15 : 55.5	−1.42	±	0.13	54	±	7	−145.2	17.77	-	28.06	23.80	19.71	18.57	17.50
MS1012419	MS	mct6V	14	00 : 46 : 32.68	+42 : 08 : 02.4	−11.02	±	0.64	87	±	9	−84.9	15.51	21.44	21.24	22.19	21.57	21.58	21.32
MS1036579	MS	mct6V	66	00 : 46 : 40.08	+42 : 11 : 18.2	−25.44	±	0.41	85	±	5	−93.4	16.42	20.00	19.97	21.08	20.49	20.46	20.26
MS1055498	MS	mct6V	130	00 : 46 : 35.27	+42 : 14 : 32.2	−6.89	±	0.12	173	±	4	−85.9	17.33	19.44	19.70	21.16	20.82	20.92	20.72
serendip1	MS	mct6V	138	00 : 46 : 37.09	+42 : 14 : 43.8	−7.32	±	0.25	159	±	7	−170.5	17.38	20.99	20.82	21.99	21.41	21.15	20.89
SG1013574	T-MS	mct6W	33	00 : 46 : 47.93	+42 : 08 : 10.4	−5.18	±	0.59	61	±	14	−138.0	15.79	24.09	23.17	22.68	21.87	21.61	21.40
AGB1016791	AGB C*	mct6W	38	00 : 46 : 19.04	+42 : 08 : 34.8	−1.15	±	0.22	52	±	9	−128.6	15.56	-	28.77	24.44	20.13	18.62	17.50
MS1021720	MS	mct6W	50	00 : 46 : 24.93	+42 : 09 : 12.8	−15.45	±	0.89	150	±	11	−62.1	15.76	20.17	20.30	21.84	21.53	21.63	21.36
MS1023445	MS	mct6W	52	00 : 46 : 35.34	+42 : 09 : 27.0	−21.48	±	0.19	121	±	3	−92.0	15.90	18.40	18.53	19.88	19.66	19.71	19.52
MS1028129	MS	mct6W	58	00 : 46 : 27.51	+42 : 10 : 06.6	−14.21	±	0.49	98	±	6	−71.4	16.02	20.12	20.19	21.17	20.93	21.00	20.85
MS1037135	MS	mct6W	82	00 : 46 : 42.87	+42 : 11 : 22.7	−14.41	±	0.38	107	±	5	−97.5	16.46	20.65	20.55	21.59	21.12	21.16	20.90
MS1041718	MS	mct6W	99	00 : 46 : 43.96	+42 : 12 : 00.4	−8.01	±	1.09	58	±	15	−106.6	16.64	20.75	20.99	22.27	22.24	22.36	22.33
MS1047936	MS	mct6W	130	00 : 46 : 45.26	+42 : 13 : 04.3	−9.6	±	3.33	74	±	59	−230.7	16.93	22.40	22.21	22.98	22.58	22.32	22.11
MS1053266	MS	mct6W	154	00 : 47 : 20.23	+42 : 14 : 05.4	−40.51	±	1.09	123	±	7	−144.5	17.67	19.82	19.95	21.18	20.99	21.07	20.93
AGB1065524	RHeB	mct6W	200	00 : 47 : 23.69	+42 : 17 : 40.7	−3.40	±	0.19	61	±	6	−326.9	18.50	-	26.80	22.78	20.52	19.76	19.02
RGB1068713	AGB C*	mct6W	216	00 : 47 : 21.37	+42 : 18 : 44.2	−10.13	±	1.88	46	±	21	−83.9	18.72	-	-	25.96	21.43	19.57	18.62
MS922906	MS	mct6X	25	00 : 46 : 52.42	+41 : 57 : 32.3	−5.24	±	0.51	62	±	10	−166.7	14.58	21.84	21.87	22.75	22.57	22.45	22.38
MS931088	MS	mct6X	37	00 : 46 : 54.63	+41 : 58 : 06.0	−32.62	±	0.82	131	±	5	−193.1	14.72	19.28	19.56	21.10	20.81	20.91	20.70
MS935185	MS	mct6X	44	00 : 46 : 39.24	+41 : 58 : 23.4	−30.85	±	0.92	156	±	7	−136.0	14.02	19.64	19.85	21.48	21.24	21.26	21.03
MS935435	MS	mct6X	46	00 : 46 : 40.07	+41 : 58 : 24.4	−1.63	±	0.08	48	±	4	−213.5	14.05	19.95	19.99	21.24	20.92	20.95	20.91
MS941562	MS	mct6X	59	00 : 46 : 28.54	+41 : 58 : 51.6	−30.36	±	1.02	111	±	8	−159.0	13.65	20.23	20.36	21.66	21.52	21.61	21.53
MS945202	MS	mct6X	68	00 : 46 : 34.22	+41 : 59 : 08.9	−11.54	±	0.29	97	±	7	−117.7	13.90	20.03	20.19	21.22	21.17	21.27	21.24
MS950839	MS	mct6X	79	00 : 46 : 29.69	+41 : 59 : 34.3	−8.43	±	1.23	58	±	17	−92.3	13.79	20.81	21.04	22.34	22.30	22.47	22.48
serendip1	RHeB	mct6X	87	00 : 46 : 27.68	+41 : 59 : 57.9	−11.23	±	3.34	36	±	34	−426.1	13.78	-	26.73	25.06	23.30	22.77	22.20
MS981758	MS	mct6X	129	00 : 46 : 14.43	+42 : 03 : 03.6	−19.76	±	2.20	105	±	25	−118.5	14.08	21.37	21.54	22.66	22.73	22.94	22.98
AGB989244	RHeB	mct6X	147	00 : 46 : 21.80	+42 : 04 : 28.0	−5.32	±	0.11	48	±	3	−24.7	14.51	-	24.90	21.94	17.63	16.23	15.50
MS1004075	MS	mct6X	193	00 : 46 : 16.42	+42 : 06 : 59.8	−49.04	±	3.36	157	±	13	−80.1	15.11	21.48	21.58	22.67	22.37	22.38	22.21

APPENDIX B: 2D SPLASH SPECTRA

Although the 2D SPLASH spectra were not used for analysis in this paper, we did use them for verifying the efficiency of our selection algorithm. Here we present a sample of four 2D SPLASH spectra, two of which are classified as Hα stars. The spectra and a description of what can be seen are given in Fig. B1, the details of each of the four objects are given in Table B1.

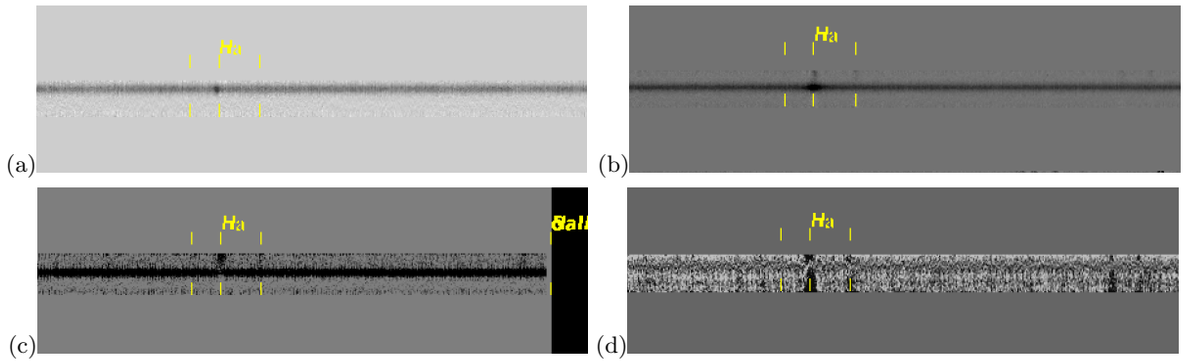

Figure B1: Four examples of 2D spectra from SPLASH to demonstrate the difference between emission-line stars (top panels) and stars surrounded by diffuse nebulous emission (bottom panels). The three yellow lines in every panel mark the wavelength of the [NII]a, Hα, and [NII]b lines respectively. The spatial extent of emission in each slit is vertical, while wavelength runs horizontally. Information on these four stars is shown in Table B1.
(a) An emission-line star within the Hα star catalogue. The stellar continuum is the thin dark horizontal line. Hα emission can be seen as a dark spot at the central yellow mark. The indication that this Hα emission is from the star and not the surrounding material is that it is the width of the stellar light and does not extend vertically from it.
(b) Another emission-line star that is also in the Hα star catalogue. This star shows the dark spot of Hα emission that is the width of the stellar light. However, this star also shows some faint spatially extended Hα emission, brightest above the horizontal band of stellar light in the image. This star has nebulous Hα emission but does not have detectable [NII] or [SII] emission and therefore has been selected as an Hα star. However, the information on the origin of Hα emission, either from the star or surrounding material, is lost in the 1D spectra. This is one of the reasons we use the visually selected list of emission-line stars, identified from the 2D spectra, in order to verify the efficiency of our selection algorithm.
(c) An example of a star that does not emit Hα but that is surrounded by nebulous Hα emission. This is shown by the spatially extended emission above the thin horizontal band of stellar light. There are also some fainter [NII] emission lines and fainter still [SII] emission lines, the second of which has been cut off due to reaching the end of the blue half of the 2D spectrum. This nebulous emission has resulted in this star being removed from the Hα star catalogue.
(d) A slightly noisier spectrum of a non-emission-line star. Here, spatially extended [NII] and [SII] emission is visible along with Hα, causing this star to be removed from our Hα star catalogue.

Table B1: Properties for the four objects whose 2D SPLASH spectra are shown in Fig. B1. The columns show the relevant panel in Fig. B1, object name, DEIMOS mask name and slit number, RA, and Dec of each object. The last column indicates whether the displayed star is in our Hα catalogue. For those that are in the catalogue, we give additional properties on the first page of Appendix A. These objects' names are enclosed in boxes in Table A1.

Panel	Object	Mask	Slit No.	RA	Dec	Hα Star
(a)	AGB154104	mct6B	193	00 : 44 : 48.54	+41 : 17 : 55.9	✓
(b)	MS179275	mct6C	64	00 : 44 : 31.66	+41 : 19 : 19.9	✓
(c)	AGB178257	mct6B	208	00 : 44 : 32.95	+41 : 19 : 16.8	✗
(d)	SG151962	mct6C	40	00 : 44 : 23.25	+41 : 17 : 48.8	✗